

LOW-MASS SEYFERT 2 GALAXIES IN THE SLOAN DIGITAL SKY SURVEY

AARON J. BARTH

Department of Physics and Astronomy, 4129 Frederick Reines Hall, University of California, Irvine, CA 92697-4575

JENNY E. GREENE¹

Department of Astrophysical Sciences, Princeton University, Princeton, NJ, 08544

AND

LUIS C. HO

The Observatories of the Carnegie Institution of Washington, 813 Santa Barbara Street, Pasadena, CA 91101

Draft version November 20, 2018

ABSTRACT

We describe a sample of low-mass Seyfert 2 galaxies selected from the Sloan Digital Sky Survey, having a median absolute magnitude of $M_g = -19.0$ mag. These galaxies are Type 2 counterparts to the Seyfert 1 galaxies with intermediate-mass black holes identified by Greene & Ho (2004). Spectra obtained with the *Echelle* *Spectrograph and Imager* at the Keck Observatory are used to determine the central stellar velocity dispersions and to examine the emission-line properties. Overall, the stellar velocity dispersions are low (~ 40 – 90 km s⁻¹), and we find 12 objects having $\sigma_* < 60$ km s⁻¹, a range where very few Seyfert 2 galaxies were previously known. The sample follows the correlation between stellar velocity dispersion and FWHM([O III]) seen in more massive Seyfert galaxies, indicating that the narrow-line FWHM values are largely determined by virial motion of gas in the central regions of the host galaxies, but the [O III] emission lines exhibit a higher incidence of redward asymmetries and double-peaked profiles than what is found in typical Seyfert samples. Using estimates of the black hole masses and AGN bolometric luminosities, we find that these galaxies are typically radiating at a high fraction of their Eddington rate, with a median $L_{\text{bol}}/L_{\text{Edd}} = 0.4$. We identify one galaxy, SDSS J110912.40+612346.7, as a Type 2 analog of the nearby dwarf Seyfert 1 galaxy NGC 4395, with a nearly identical narrow-line spectrum and a dwarf spiral host of only $M_g = -16.8$ mag. The close similarities between these two objects suggest that the obscuring torus of AGN unification models may persist even at the lowest luminosities seen among Seyfert galaxies, below $L_{\text{bol}} = 10^{41}$ ergs s⁻¹. Spectropolarimetry observations of four objects do not reveal any evidence for polarized broad-line emission, but SDSS J110912.40+612346.7 has a continuum polarization significantly in excess of the expected Galactic foreground polarization, possibly indicative of scattered light from a hidden nucleus. Forthcoming observations of this sample, including X-ray and mid-infrared spectroscopy, can provide new tests of the obscuring torus model for active galaxies at low luminosities.

Subject headings: galaxies: active — galaxies: kinematics and dynamics — galaxies: nuclei — galaxies: Seyfert

1. INTRODUCTION

The majority of active galactic nuclei (AGNs) are found in giant galaxies with substantial bulges, and there is a dramatic drop in the AGN fraction for late Hubble types (Ho et al. 1997) and for host galaxies with stellar masses below $\sim 10^{10} M_\odot$ (Kauffmann et al. 2003b). This trend is consistent with the generally accepted scenario in which black hole growth and bulge growth are closely coupled, as expected from the correlations between black hole mass and bulge mass (Kormendy & Richstone 1995), and between black hole mass and stellar velocity dispersion (the $M_{\text{BH}} - \sigma_*$ relation; Ferrarese & Merritt 2000; Gebhardt et al. 2000). The low AGN fraction in late-type and low-mass galaxies arises from a combination of factors. Perhaps most important, the black hole occupation fraction in low-mass galaxies is apparently below unity, as demonstrated by the stellar-dynamical non-detections of central black holes in the Local Group galaxies M33 (Gebhardt et al. 2001; Merritt et al. 2001) and NGC 205 (Valluri et al. 2005). For those late-type galaxies that do contain a central black hole, shallow central gravitational potential wells may

lead to a low efficiency for fueling black hole accretion. A low-mass black hole ($\lesssim 10^6 M_\odot$), even if radiating at its Eddington rate, cannot produce a very luminous AGN, and such objects can only be readily detected as AGNs if they are fairly nearby. In optical surveys, dust extinction and blending with circumnuclear star-forming regions can further hinder the detection of low-luminosity active nuclei in late-type spirals.

If the $M_{\text{BH}} - \sigma_*$ relation continues toward low masses, then a black hole of $10^6 M_\odot$ would correspond to a host galaxy velocity dispersion of $\sigma_* \approx 60$ km s⁻¹ (Tremaine et al. 2002). Thus, to explore the intermediate-mass regime for black holes, it is particularly interesting to search for AGN host galaxies having $\sigma_* < 60$ km s⁻¹. Such objects are known to exist, but they are rare. Prior to the Sloan Digital Sky Survey (SDSS), there were only two nearby examples of dwarf galaxies known to contain Seyfert 1 nuclei: POX 52, a dE galaxy with $\sigma_* = 36 \pm 5$ km s⁻¹ (Kunth et al. 1987; Barth et al. 2004), and NGC 4395, an Sd-type spiral with a central velocity dispersion of $\sigma_* \lesssim 30$ km s⁻¹ (Filippenko & Sargent 1989; Filippenko & Ho 2003). The availability of SDSS has made it possible for the first time to search systematically for more examples of AGNs with low-mass black holes and small central

¹ Hubble Fellow

velocity dispersions. Greene & Ho (2004; hereinafter GH04) carried out the first such survey using Data Release 1 of the SDSS, identifying 19 Seyfert 1 galaxies as likely candidates for having $M_{\text{BH}} < 10^6 M_{\odot}$. Although host galaxy properties were not considered in the sample selection, the hosts for this sample turned out to be galaxies of relatively low luminosity, on average about 1 mag fainter than L^* . Barth et al. (2005) measured stellar velocity dispersions for many of the galaxies in this sample and found that they are also low ($\sim 35 - 80 \text{ km s}^{-1}$) and fall close to the local $M_{\text{BH}} - \sigma_*$ relation extrapolated toward lower masses.

Most previous searches for low-mass AGNs have concentrated on Type 1 (broad-lined) objects (Greene & Ho 2004, 2007; Dong et al. 2006) because the broad-line widths and AGN continuum luminosity can be used to estimate the black hole mass. However, at low luminosities, most Seyferts are Type 2 objects (Ho et al. 1997; Hao et al. 2005b), and a full determination of the demographics of AGNs with low-mass black holes must take into account the Type 2 population. Furthermore, without the glare of a bright AGN point source, the host galaxies of Seyfert 2s are more easily studied. This can make it possible to examine the central stellar populations and star formation histories of Seyfert 2 host galaxies in a level of detail that would be impossible for Type 1 AGNs (Kauffmann et al. 2003b; Heckman et al. 2004). Since searches for broad-lined AGNs require both the flux and the width of a broad emission line (such as $\text{H}\alpha$) to be above some detection threshold, surveys for Type 2 AGNs based on measurements of narrow emission lines can potentially probe lower AGN luminosities, and therefore may be sensitive to AGNs in smaller host galaxies, or containing black holes of lower mass than those that can be found in Seyfert 1 surveys. Optical spectroscopic surveys such as the Palomar survey (Ho et al. 1997) have previously identified some examples of very low-luminosity Seyfert 2 nuclei in late-type galaxies, such as the Sc galaxy NGC 1058, which has a central velocity dispersion of only $31 \pm 6 \text{ km s}^{-1}$ (Barth et al. 2002). Other strategies for finding obscured AGNs, such as mid-infrared searches for high-ionization coronal line emission from obscured active nuclei (Satyapal et al. 2007), have contributed further evidence for black holes in late-type spirals. Since stellar-dynamical searches for low-mass black holes are limited to very nearby galaxies (within a few Mpc at best), AGN surveys remain the best way to examine the demographics of these objects, and to determine the properties of the host galaxies in which low-mass black holes form and grow.

This paper describes new observations of a set of Seyfert 2 galaxies selected from Data Release 2 of the Sloan Digital Sky Survey (Abazajian et al. 2004, SDSS DR2) to have host galaxies with relatively low luminosities and small central velocity dispersions. We select galaxies spectroscopically identified as having Seyfert 2 nuclei (rather than LINER or AGN/starburst transition or composite types), in order to focus on objects having nuclear emission-line spectra that are clearly and unambiguously dominated by an accretion-powered AGN. These galaxies are in many respects Type 2 counterparts of the low-mass Seyfert 1 sample found by GH04, although the two samples are selected by very different criteria. Most of the objects in both of these samples are not small or faint enough to be considered dwarf galaxies, but the objects described here are sub- L^* galaxies that occupy ranges in mass, luminosity, and central velocity dispersion where very few Type 2 AGNs were known before SDSS.

We present measurements of the properties of these galax-

ies from high-resolution spectra taken at the Keck Observatory. The small-aperture, high-resolution Keck spectra make it possible to confirm the AGN classification of these galaxies, to detect weak emission-line features and search for faint broad-line components, to measure stellar velocity dispersions, and to fully resolve the profiles of the narrow emission lines and measure accurate linewidths. We discuss the properties of these galaxies and the Seyfert 1s from the GH04 sample in the context of unified models of AGNs. We also describe a search for polarized broad-line and continuum emission in four of these low-mass Seyfert 2 galaxies. In this paper, distance-dependent quantities are calculated assuming $H_0 = 72 \text{ km s}^{-1} \text{ Mpc}^{-1}$, $\Omega_m = 0.3$, and $\Omega_{\Lambda} = 0.7$.

2. SAMPLE SELECTION

Our goal for this project was to identify Seyfert 2 galaxies having low velocity dispersions, as Type 2 counterparts to the Seyfert 1 galaxies identified by GH04. We initially searched the SDSS DR2 archives for narrow emission-line galaxies at $z < 0.1$ with emission-line ratios matching a Seyfert 2 classification (as described below), and host galaxies with absolute magnitude fainter than $M_g = -20$ mag. In the GH04 Seyfert 1 sample, the host galaxy absolute magnitudes ranged from $M_g = -17.8$ to -20.6 mag with a median of -18.9 mag.

The line-ratio selection was based on two criteria:

$$\log([\text{O III}]/\text{H}\beta) > 0.61 / \{\log([\text{N II}]/\text{H}\alpha) - 0.47\} + 1.19,$$

and

$$[\text{O III}]/\text{H}\beta > 3,$$

where $[\text{O III}]$ and $[\text{N II}]$ refer to the fluxes of the $[\text{O III}] \lambda 5007$ and $[\text{N II}] \lambda 6583$ emission lines, respectively. The first criterion represents the “maximum starburst line” of Kewley et al. (2001), which separates the H II region and AGN branches of a Baldwin et al. (1981) “BPT” diagnostic diagram. The location of this maximum starburst line was slightly modified in later work by Kauffmann et al. (2003b) and Kewley et al. (2006), but our sample is not affected by this change. The second criterion was used to identify high-excitation Seyfert galaxies and exclude LINERs or objects with LINER/H II transition-type spectra, following traditional classification criteria (Ho et al. 1997).

After we had begun some initial Keck observations, the SDSS DR2 galaxy catalogs of G. Kauffmann and collaborators (the MPA/JHU catalogs), based on work described by Kauffmann et al. (2003a,b), became available to the public.² The MPA/JHU AGN catalogs include narrow emission-line galaxies falling above and to the right of the maximum starburst line in the $[\text{O III}]/\text{H}\beta$ vs. $[\text{N II}]/\text{H}\alpha$ diagram, so their AGN samples contain both Seyferts and LINERs. For a description of their AGN sample selection and classification criteria, see Kauffmann et al. (2003b), which was based on the SDSS DR1 sample. We then used these catalogs to select further candidates, and most of the objects we had initially selected from the SDSS archives were included in the MPA/JHU DR2 AGN sample.

The MPA/JHU catalogs are an excellent resource for statistical studies of nearby narrow-line AGN populations, because of the very large sample size (33,589 AGNs in DR2 and 88,178 in the later DR4 catalog) and the inclusion of additional data on the host galaxies including stellar masses, stellar velocity dispersions, and the absorption-line indices $\text{H}\delta_A$

² Updated versions of the MPA/JHU catalogs described by Kauffmann et al. are available at <http://www.mpa-garching.mpg.de/SDSS>.

and $D_n(4000)$, which are sensitive to the galaxy’s star formation history (see Kauffmann et al. 2003a,b, for details). To ensure that our sample contained galaxies with well-determined AGN classifications, we further selected only galaxies having measurements of [O III] flux with $S/N > 10$ based on the DR2 emission line catalog. Several of the objects in our sample have also been previously identified as Seyferts based on SDSS spectra by Hao et al. (2005a), but a literature search revealed that only two galaxies in our sample (1440+0247 and 1032+6502) were identified as AGNs prior to the SDSS. A few cases of galaxies with possible broad H α emission lines, that otherwise met our selection criteria, were included in the sample. As described below, we used the Keck spectra to test the reality of the broad-line emission.

A total of 29 galaxies meeting these selection criteria were observed at Keck. The sample properties are described in Table 1, and Figure 1 displays SDSS images of each object. The redshifts range from $z = 0.0056$ to 0.0712 , with a median of 0.042 . Since the size of this Keck sample was determined by the available telescope time and the practical need to observe objects distributed over a range of right ascension, the set of objects in this study is not a statistically complete sample, but they should be generally representative of the small population of Seyfert 2 nuclei in sub- L^* host galaxies in SDSS. In Table 1, the absolute g -band magnitudes are K -corrected to $z = 0$ using M. Blanton’s *kcorrect* IDL code (version 4_1_4; Blanton & Roweis 2007) and corrected for Galactic extinction using the dust maps of Schlegel et al. (1998).

We note that the absolute magnitudes listed in Table 1 are based on the SDSS Petrosian magnitudes (see Strauss et al. 2002). For most objects in this sample, the Petrosian aperture magnitudes agreed to within ~ 0.1 mag with the “model” magnitudes based on the best-fitting de Vaucouleurs or exponential model. The magnitudes are not corrected for internal extinction, since for most objects in the sample there is insufficient morphological information to make such a correction.

For the objects selected from the MPA/JHU DR2 catalog, the host galaxy stellar masses ranged from $\log(M_*/M_\odot) = 8.1$ to 10.5 , with a median value of 9.8 . Although the MPA/JHU DR2 and DR4 AGN catalogs contain a substantial number of AGN candidates with extremely low stellar masses (i.e., below $10^9 M_\odot$), we found that the vast majority of these objects do not satisfy the selection criteria given above. The MPA/JHU DR2 AGN catalog contained 90 objects with $\log(M_*/M_\odot) < 9.5$ and 17 with $\log(M_*/M_\odot) < 9.0$. Inspection of the SDSS spectra of these objects revealed that most of them have LINER or transition-type spectra, or very weak emission lines with such low equivalent width that the AGN classification is somewhat ambiguous. There were also a few cases of nearby giant galaxies (including NGC 5775 and NGC 3166) being listed in the AGN catalog with very low host galaxy masses of $\log(M_*/M_\odot) < 9$. These appear to be objects for which the SDSS catalog magnitudes include only the galaxy’s nucleus, resulting in a severe underestimate of the total stellar mass. The situation for the DR4 AGN catalog is similar: at $\log(M_*/M_\odot) < 9$, there are 52 objects in this catalog, most of which are either LINER or transition-type objects, objects with emission lines of very low equivalent width, or large nearby galaxies with incorrect total magnitudes. Only a small fraction of the objects in this mass range ($\lesssim 10\%$) would satisfy our Seyfert selection criteria. Thus, the population statistics of AGNs with extremely low-mass host galaxies in these catalogs should be treated with some caution.

3. OBSERVATIONS

3.1. ESI Spectroscopy

The spectroscopic observations described here were obtained with the ESI spectrograph (Sheinis et al. 2002) on the Keck-II telescope. Most of the this sample was observed during 2005 May 16–17, with a few objects observed during runs on 2003 November 23–24 and 2004 October 9–10. We used the ESI echelle mode with a $0''.75$ -wide slit, resulting in an instrumental dispersion of $\sigma_i \approx 22 \text{ km s}^{-1}$ and a total wavelength coverage of $3850\text{--}11000 \text{ \AA}$. The pixel scale in the dispersion direction is $11.5 \text{ km s}^{-1} \text{ pix}^{-1}$. The slit was held at a fixed position angle during each observation, corresponding approximately to the parallactic angle for the midpoint of the exposure. Exposure times for the galaxies ranged from 900 to 3600 s (Table 2). Seeing was mostly in the range $0''.7\text{--}1''.0$. One or more flux standards were observed during each night, and several velocity template stars of spectral type ranging from G8III to K4III, and also a few A0V stars, were observed during twilight. For wavelength calibration, exposures of HgNe, Xe, and CuAr comparison lamp spectra were taken.

The spectra were bias-subtracted, flattened, and extracted with a fixed extraction width of $1''$. Standard (not optimally weighted) extractions were used, because optimal extraction routines tend to truncate the peaks of emission-line profiles when the emission-line regions have a different spatial extent from the stellar continuum. The extracted spectra for the individual echelle orders were wavelength-calibrated and flux-calibrated, and corrected for telluric absorption by dividing by a normalized spectrum of a white dwarf star observed on the same night. Error spectra were also extracted and propagated through the full sequence of calibrations. Finally, the 10 echelle orders were combined into a single spectrum for each galaxy, using a weighted average to combine the overlap regions between orders. Systematic offsets between the flux scales of adjacent orders within the overlap regions were typically smaller than 2.5%. The combined spectra were binned to a logarithmic wavelength scale with a binsize of $\Delta[\log(\lambda/\text{\AA})] = 1.665 \times 10^{-5}$. Figure 2 displays the central portion of the ESI spectra.

3.2. Spectropolarimetry

We obtained spectropolarimetry observations of four objects using the LRIS polarimeter (LRISp; Goodrich et al. 1995) on the Keck I telescope on the night of 2005 December 30, in clear conditions with $0''.7$ seeing. The instrumental setup consisted of a 400 lines mm^{-1} grism on the blue side of the spectrograph, covering $3200\text{--}5700 \text{ \AA}$ at $1.09 \text{ \AA pixel}^{-1}$, and a 600 lines mm^{-1} grating on the red side, covering $5500\text{--}8000 \text{ \AA}$ at $1.28 \text{ \AA pixel}^{-1}$. A $1''$ -wide slit was used, and the slit was oriented along the parallactic angle for the midpoint of the exposure sequence. Observations of each object consisted of a sequence of four exposures with the half-wave plate oriented at 0, 45, 22.5, and 67.5 degrees. For three galaxies (0119+0037, 0214-0016, and 0947+5349), one exposure set was taken, for a total on-source exposure of one hour, and for the galaxy 1109+6123 we obtained two exposure sequences for a total of two hours of integration. Calibrations were performed using observations of polarized and unpolarized standards (Mathewson & Ford 1970; Clemens & Tapia 1990; Turnshek et al. 1990), and flux standard stars observed during twilight. Data reduction and polarization analysis followed the methods outlined by Miller et al. (1988), using a

3''-wide spectral extraction. The null standard star HD 57702 was found to be unpolarized to within 0.08% in both the blue and red side extractions, in close agreement with other recent measurements done with LRISp (Leonard et al. 2002).

4. RESULTS AND DISCUSSION

4.1. Emission-Line Diagnostics

Before measurement of the emission lines from the ESI spectra, we applied a simple starlight subtraction procedure to remove the stellar continuum from each spectrum. The fitting routine used a linear combination of two stellar templates, a K giant and an A0V star, from the library of stellar spectra observed on the same nights as the galaxies. A featureless, power-law continuum component was added, and the continuum was velocity-broadened by convolution with a Gaussian kernel and fitted to the galaxy spectrum using a Levenberg-Marquardt minimization routine. The free parameters in the fit included the normalization of the two stellar spectra and the featureless continuum, the stellar velocity dispersion, the power-law index of the featureless continuum, and the reddening (assuming a Galactic extinction law). Spectral regions containing emission lines were masked out in the fit. This procedure was repeated for each galaxy using several different late-type giant stars and A0V stars to find the best-fitting combination. While the starlight-subtracted spectra of some galaxies still contained broad residual features or small jumps at the boundaries between echelle orders, this procedure generally yielded a good fit to the continuum shape and the strong stellar features over the region $\sim 4000\text{--}7000\text{ \AA}$, as illustrated in Figure 3. Although these fits give an estimate of the stellar velocity dispersion, better measurements of the velocity dispersions are determined from fits to smaller spectral windows in individual echelle orders containing strong absorption-line features (as described below), and we used these global fits primarily for purposes of starlight subtraction to obtain the emission-line spectra.

The fluxes of the $H\alpha$, $H\beta$, [O III] $\lambda 5007$, [O I] $\lambda 6300$, [N II] $\lambda\lambda 6548, 6583$, and [S II] $\lambda\lambda 6716, 6731$ emission lines were measured by Gaussian fitting to the line profiles in the starlight-subtracted spectra. Each line was first fit with a single Gaussian component, and if there were significant systematic residuals, a second Gaussian component was added. For the [N II] and [S II] doublets, the wavelength separations between each component were fixed to their laboratory values, and the velocity widths of the corresponding components for each line were held to be equal. The flux ratio of the [N II] $\lambda 6583$ and 6548 lines was set to 2.96:1.

From inspection of the SDSS spectra of these galaxies, four objects appeared to be likely or possible candidates for having broad $H\alpha$ emission, and we used a single Gaussian component to fit the broad line (Figure 4). Two of the broad $H\alpha$ candidates were the two objects that were not selected from the MPA/JHU catalog: 1032+6502 and 1440+0247. In the case of 1032+6502, inspection of the starlight-subtracted ESI spectrum clearly confirms the reality of the broad $H\alpha$ feature, and the broad component in the ESI data has $\text{FWHM} = 3020 \pm 33\text{ km s}^{-1}$. The result of the model fit for 1440+0247 is somewhat more ambiguous. A fit using a double-Gaussian narrow-line model left very weak residuals in the wings of $H\alpha$ but the residuals only extended in wavelength as far as the gaps between $H\alpha$ and the [N II] lines on either side. Adding a broad $H\alpha$ component marginally improved the quality of the fit, and the best-fitting model had a broad component width

of $\text{FWHM} = 1040 \pm 20\text{ km s}^{-1}$. Given the narrowness and low amplitude of this possible broad component, it is not clear whether this represents emission from a distinct broad-line region (BLR), and we consider it a tentative detection at most.

The other two broad $H\alpha$ candidates were selected from the MPA/JHU catalog. The first, 0110+0026 has an obvious and strong broad $H\alpha$ emission line that is clearly visible in the SDSS spectrum and confirmed in the ESI data, with $\text{FWHM} = 5170\text{ km s}^{-1}$. The other candidate is 1629+4254; for this object both the SDSS and ESI spectra show broad bases to all of the narrow emission lines. Fitting the lines with a narrow core and broad redshifted base for each narrow line, we were able to reproduce the overall shape of the $H\alpha$ + [N II] blend adequately. Although the double-Gaussian model does not perfectly reproduce the narrow-line profiles, the broad bases are present on all of the forbidden lines and there does not appear to be any need to include a separate broad $H\alpha$ component in the fit. For the remaining objects, no broad-line component was required to fit the $H\alpha$ + [N II] spectral region in the ESI spectra.

Figure 5 shows the location of the galaxies in this sample (measured from the Keck ESI spectra) on line-ratio diagnostic diagrams, as well as the GH04 Seyfert 1 sample and the nearby AGNs NGC 4395 and POX 52. The AGN classifications are essentially unchanged between the SDSS 3''-diameter fiber measurements and the Keck $0.''75 \times 1''$ aperture extractions. In the smaller Keck aperture, only one object falls just slightly below our [O III]/ $H\beta$ selection threshold.

In the diagram of [O III]/ $H\beta$ vs. [N II]/ $H\alpha$, the galaxies in this sample, as well as the GH04 sample, deviate systematically away from the main locus of SDSS Seyfert 2 galaxies, toward lower values of [N II]/ $H\alpha$. NGC 4395 and POX 52 also lie in this same sparsely populated region of the diagram, around $\log([\text{N II}]/H\alpha) \approx -0.5$ and $\log([\text{O III}]/H\beta) \approx 1$. Photoionization modeling by Kraemer et al. (1999) and Groves et al. (2006) has shown that this region of the diagnostic diagram is occupied by Seyferts having lower narrow-line region (NLR) metallicity than in typical Seyfert nuclei; for high-excitation AGNs, decreasing the metallicity moves the line ratios systematically leftward on the diagram. This region of the diagram is nearly empty, relative to the main Seyfert branch, as a result of the low incidence of active nuclei in low-metallicity galaxies. In the models of Groves et al. (2006), the majority of Seyferts have NLR metallicity between ~ 2 and $4Z_{\odot}$, while NGC 4395 and POX 52, and the more extreme objects in our sample and the GH04 sample, fall in the region of the diagram corresponding to $Z \approx Z_{\odot}$. At still lower metallicities, below $0.5Z_{\odot}$, the AGN and H II sequences overlap, and additional diagnostics would be needed to distinguish AGN from star-forming nuclei. However, we note that the multi-component photoionization models for NGC 4395 described by Kraemer et al. (1999) found a good match to the narrow-line spectrum for a metallicity of $0.5Z_{\odot}$ overall and an N/H ratio of 1/6 solar. Regardless of the exact value of the metal abundances in these galaxies, the work of Groves et al. (2006) clearly demonstrates that AGN selection based on low host galaxy mass efficiently identifies AGNs with lower than average metallicity, and our sample follows this trend. In our sample, the object that deviates most from the normal Seyfert branch in the BPT diagram is 1109+6123, which is also the faintest and least massive galaxy in the sample.

We searched for high-ionization coronal line emission in the spectra, as additional indicators of AGN activity. The galaxy 1440+0247 shows a range of coronal lines including

[Fe VI] λ 5177, [Fe VII] (λ 5158, 5720, and 6087 Å), [Fe X] λ 6374, and [Fe XI] λ 7802 (Figure 6). Its spectrum is extremely similar to that of NGC 4395 (Filippenko & Sargent 1989; Kraemer et al. 1999) aside from the relative weakness of the broad H α emission. The Type 1 object 1032+6502 also has weak [Fe VII] and [Fe X] emission. Among the remaining Type 2 objects in the sample, these high-excitation Fe features are seen in only one object, 0214–0016. The LRISp spectra extend farther to the blue than the ESI data, and three of the four LRISp targets (0214–0016, 0947+5349, and 1109+6123) have [Ne V] λ 3426 emission in their spectra.

Since the individual ESI spectra have rather low S/N at the blue and red ends, we created a composite Seyfert 2 spectrum by summing the individual spectra (excluding the three objects with definite or possible broad H α emission), corrected for Galactic extinction and weighted by the S/N of each spectrum. Figure 7 shows the composite spectrum, with the starlight subtraction procedure applied as described above. The best-fitting K+A spectral model for the composite spectrum shows deep Balmer absorption, and reveals emission lines that are difficult to detect clearly in many of the noisy individual spectra, including [Ne III] λ 3868, 3967, [Fe VII] λ 6086, and the [S III] λ 9069, 9532 lines at the red end. We measured emission line fluxes from the composite spectrum; when necessary, in regions where the starlight subtraction left significant residuals a spline was first fitted to the local continuum and subtracted in order to flatten the continuum. Emission-line fluxes measured from the composite spectrum are given in Table 3.

4.2. [O III] Profiles

Following methods similar to those described by Greene & Ho (2005), we measured the linewidths of strong emission lines from fits of single or double-Gaussian models to each line. We focus on the [O III] λ 5007 emission line since this is the strongest forbidden line in the spectra and it is uncontaminated by underlying stellar absorption or blending with other emission lines. For three galaxies in the sample, the [O III] profiles were adequately modeled by single Gaussian components with no strong systematic residuals. In all other cases, two Gaussian components were used to model each narrow emission line. This type of line-profile decomposition is often interpreted in terms of a core component dominated by virial motions and a wind-dominated wing component (e.g., Greene & Ho 2005), although some objects in our sample have more complex profiles that do not fit this simple qualitative description. Figure 8 shows the [O III] λ 5007 profiles for the sample.

The [O III] profiles exhibit a greater degree of diversity than seen in previous SDSS samples. It has long been known that blueward asymmetries on [O III] profiles are much more common than redward asymmetries (e.g., Osterbrock & Mathews 1986). In the large sample of 1749 SDSS Seyfert 2 spectra studied by Greene & Ho (2005), most of the narrow-line profiles were well described by a narrow core component plus a low-amplitude, blueshifted “wing” component. The wing component was found to be redshifted relative to the core in only 6% of the objects. In contrast, our sample seems to have an unusually large fraction of objects with redward asymmetries. Eight objects, or 28% of the sample, have red-asymmetric profiles, in the sense of having a single dominant peak with an excess of flux on the red side of the peak relative to the blue side. Some other objects (such as 1112+5529 and 1432+0046) have profiles that are well fit by the double-Gaussian model but for which the model components cannot

be individually labeled as core or wing components, because the broader component contains the majority of the line flux and the velocity difference between the two components is small. Either blueward or redward asymmetries can be interpreted as resulting from radial motion (inflow or outflow) of clouds combined with the presence of dust, either within the clouds themselves or in a surrounding medium. In the more common situation of blueward asymmetries, a likely explanation is outflowing motion of clouds in a dusty medium, in which the redshifted clouds on the far side of the galaxy nucleus are behind a larger absorbing column of dust (e.g., Heckman et al. 1981). However, there are possible geometric arrangements of an outflow and dust screen that would lead to a redward asymmetry as well, if the outflow direction is not restricted to be perpendicular to the plane of the dust screen. Alternatively, if the dust is contained within the NLR clouds themselves, then the emission from a cloud would be strongest in the direction facing the central ionizing source, and in an outflow we would have a more direct view of the ionized faces of the redshifted clouds on the far side of the nucleus, rather than the ionized faces of the blueshifted clouds, leading to a redward asymmetry on the line profiles. As discussed by Whittle (1985), the line profiles do not contain sufficient information to uniquely determine the kinematic state of the NLR or the distribution of dust within it.

More surprising is the detection of double-peaked forbidden-line profiles in three objects. Two galaxies, 0343–0735 and 1006+4456, have fairly symmetric double-peaked [O III] profiles with well-resolved peaks. The peak-to-peak velocity separation of the two components in these objects is 115 and 275 km s⁻¹, respectively. The most spectacular example is 1629+4254, which contains a narrow core component having FWHM = 78 km s⁻¹ and a very broad, redshifted wing component with a peak velocity separation of 223 km s⁻¹ and FWHM = 589 km s⁻¹. Additionally, a marginally resolved second peak is visible on the red shoulder of the [O III] line profile in 0914+0238. For comparison, the Greene & Ho (2005) study found double-peaked profiles in only about 1% of SDSS Seyfert 2 spectra. The relatively high incidence of double-peaked profiles in this sample likely results from a combination of the high spectral resolution of ESI, the smaller spectroscopic aperture of the Keck observations, and the low intrinsic linewidths for the individual velocity components in these low-mass galaxies. In the SDSS spectra, velocity splittings much smaller than the instrumental FWHM of \sim 170 km s⁻¹ would be unresolved, and only one of these four objects (1006+4456) exhibits double-peaked lines in the lower-resolution SDSS data. The SDSS spectrum for 1629+4254 shows a single-peaked but strongly red-asymmetric [O III] profile.

Double-peaked narrow emission lines can arise from a disk-like NLR, from outflows, or possibly from a binary AGN with two distinct NLRs (e.g., Zhou et al. 2004). While a fast outflow is the most likely explanation for the extremely broad and asymmetric profile seen in 1629+4254, the galaxies 0343–0735 and 1006+4456 have more symmetric double-peaked [O III] profiles suggestive of a disklike emitting region. The possibility of a disklike NLR would be difficult to test directly by spatially resolved kinematics or morphology, however, since the diameter of such a disk would be too small to resolve directly in these galaxies.

The linewidths for [O III] were characterized by two different quantities: the line dispersion (that is, the second moment of the line profile) and the full-width at half-maximum.

Given the limited S/N in the profile wings in some objects, we chose to measure the linewidth parameters from the fitted model profile rather than from the data itself, following methods similar to those used by Greene & Ho (2005). The line dispersion is given by

$$\sigma_{\text{line}}^2 = \left(\frac{c}{\lambda_0}\right)^2 \frac{\int (\lambda - \lambda_0)^2 f_\lambda d\lambda}{\int f_\lambda d\lambda},$$

where λ_0 is the flux-weighted mean wavelength of the emission line. The FWHM was measured as the full velocity width at half of the peak flux density of the modeled line profile. In the case of a Gaussian profile, $\sigma = \text{FWHM}/2.35$. For line profiles having the prototypical core/wing structure, the FWHM is primarily sensitive to the width of the narrow core component, and the ratio of σ to $(\text{FWHM}/2.35)$ gives a measure of the relative prominence of the line wings.

The instrumental dispersion was removed by subtracting it in quadrature from the measured line dispersions, according to $\sigma_{\text{line}}^2 = \sigma_{\text{obs}}^2 - \sigma_{\text{inst}}^2$, and for the FWHM values we subtracted $(2.35\sigma_{\text{inst}})$ in quadrature from the measured values. Uncertainties on FWHM and σ were determined by Monte Carlo simulations. Starting with the single or double-Gaussian fit parameters for each galaxy, we created 1000 realizations of the line profile, drawing the amplitude, width, and centroid of each Gaussian component randomly from a normal distribution based on the fitting uncertainties from the original profile fit. Noise was then added to match the S/N of the original spectrum, and the simulated profile was fitted in the same manner as the original spectrum. The uncertainty on the line dispersion or FWHM was then taken to be the standard deviation of linewidth values measured from the set of simulated profiles. The results are listed in Table 2. The FWHM values for the [S II] lines, measured in the same manner, are also listed.

As expected for galaxies of relatively low mass, the narrow emission lines in these galaxies are much narrower than those of more luminous, classical Seyfert 2 galaxies. Excluding the three strongly double-peaked objects, the median values of $\text{FWHM}_{[\text{O III}]}$ and $\sigma_{[\text{O III}]}$ are 132 and 87 km s⁻¹, respectively, and the narrowest-lined object, 1109+6123, has $\text{FWHM}_{[\text{O III}]} = 66$ km s⁻¹.

4.3. Stellar Velocity Dispersions

Stellar velocity dispersions (σ_*) were measured from the ESI spectra by direct fitting of velocity-broadened stellar templates, following the method described by Barth et al. (2002). Although the starlight subtraction procedure described above in §4.2 yielded an estimate of the stellar velocity dispersion, the starlight subtraction fits were performed over the entire wavelength range of the data. For accurate measurement of velocity dispersions it is critical to perform the measurements over a restricted wavelength range containing strong stellar absorption features. It is also critical to mask out wavelengths containing narrow emission lines so that they do not affect the dispersion measurements. To eliminate any potential issues of mismatch in spectral resolution between echelle orders, we carried out the velocity dispersion measurements using spectra from a single echelle order.

Measurements were performed independently over two wavelength ranges, as illustrated in Figure 9: a blue region (5130–5470) including the strong Mg b and Fe 5270 lines, and the Ca II triplet region (8450–8700 Å). When visible in the spectra or in the fit residuals, emission lines such as [N I]

$\lambda\lambda 5199, 5201$ were masked out from the fits. For the velocity dispersion measurements, the model fits consisted of a template star broadened by a Gaussian in velocity, diluted by addition of a featureless continuum (modeled by a quadratic polynomial in this case), and multiplied by another quadratic polynomial that allows for reddening or systematic flux calibration differences between the galaxy and template star observations. The velocity dispersion was measured using template stars observed on the same night as each galaxy. Uncertainties on the velocity dispersions were determined as the sum in quadrature of the formal fitting errors from the best-fitting model and the standard deviation of the velocity dispersions found from all available templates. The final velocity dispersion values listed in Table 2 are the weighted averages of the red and blue measurements. As expected for galaxies of low stellar mass, the velocity dispersions for this sample are low, ranging from 39 to 94 km s⁻¹ with a median value of 63 km s⁻¹, and with 12 objects having $\sigma_* < 60$ km s⁻¹. For two objects, 1053+0410 and 1109+6123, the continuum S/N was too low to permit a measurement of σ_* .

These measurements give the dispersion of the line-of-sight velocity profile for the integrated galaxy light falling in the ESI slit and extraction aperture, and represent a combination of light from bulges or pseudobulges, disks, and possibly central star clusters. Higher-resolution images would be needed in order to determine the relative contributions of starlight from the various structural components. Using bulge-disk decompositions of the GH04 Seyfert 1 sample from *Hubble Space Telescope* (HST) imaging, Greene, Ho, & Barth (2008) found that the measured dispersions from Barth et al. (2005) were dominated by bulge light for those systems with detected bulges, but that in some host galaxies without detected bulges the measured dispersion was likely dominated by disk starlight. In either case, the fact that the GH04 Seyfert 1 galaxies fall close to the $M_{\text{BH}} - \sigma_*$ relation extrapolated to low masses means that the central stellar velocity dispersion measured in a $\sim 1''$ aperture, regardless of its origin, is still reasonably well correlated with black hole mass for these low-mass AGNs.

4.4. Comparison between Stellar and Gas Linewidths

With measurements of both stellar velocity dispersions and forbidden-line widths, we can examine whether the correlation between σ_* and [O III] linewidth, well established for typical Seyfert 2 galaxies (Nelson & Whittle 1996), continues to hold for these low-dispersion Seyferts. This issue has attracted considerable recent attention as a result of the potential utility of the [O III] linewidth as a substitute for σ_* in studies of the $M_{\text{BH}} - \sigma_*$ relation for certain subclasses of AGNs for which σ_* can be difficult or impossible to measure directly (Wang & Lu 2001; Shields et al. 2003; Grupe & Mathur 2004; Bian & Zhao 2004; Salviander et al. 2007; Bian et al. 2006). For a large sample of nearby Seyferts (mostly of Type 2), Nelson & Whittle (1996) found that the mean value of $\text{FWHM}_{[\text{O III}]} / (2.35\sigma_*)$ was very close to unity, but that for individual objects there was considerable scatter in the relationship between stellar and gas linewidths. Using SDSS spectra of a large sample of low-redshift Seyfert 2 galaxies, Greene & Ho (2005) confirmed this general trend. Additionally, they found that Seyfert 2 galaxies tend to have an “excess” emission-line velocity dispersion, over and above the stellar velocity dispersion, that increases as a function of $L_{\text{bol}}/L_{\text{Edd}}$, and that the [O III] “core” component width (based on a double-Gaussian decomposition) is a better predictor of

σ_* than the dispersion of the full [O III] profile. These trends are consistent with a scenario in which the linewidth of the NLR core component is primarily set by virial motion of gas in the host galaxy’s bulge, while the increasing excess linewidth with Eddington ratio reflects an increasing prevalence of winds or outflows in highly accreting objects. Since the SDSS spectra themselves cannot be used to measure stellar or emission-line widths for features with $\sigma \lesssim 70 \text{ km s}^{-1}$, our sample allows us to extend these relationships to galaxies with lower velocity dispersions.

Figure 10 shows the comparison between stellar and [O III] linewidths, excluding the two galaxies for which σ_* could not be measured as well as the three objects with strongly double-peaked [O III] profiles. We examine both $\sigma_{[\text{O III}]}$, which is sensitive to the profile wings, as well as $\text{FWHM}_{[\text{O III}]}$. In our sample, the distinction between core and wing components is not always obvious from the line-profile fits, and we cannot uniformly select a core component from the double-Gaussian profile fits, but the FWHM values essentially reflect the width of the line core. The measured values of $\sigma_{[\text{O III}]}$ are systematically higher than σ_* , while the values of $\text{FWHM}_{[\text{O III}]} / 2.35$ track σ_* much more closely. To quantify this comparison, following Nelson & Whittle (1996) and Greene & Ho (2005), we measure the quantities $\Delta W = \log(\text{FWHM}_{[\text{O III}]} / 2.35) - \log(\sigma_*)$, and $\Delta\sigma = \log \sigma_{[\text{O III}]} - \log \sigma_*$. For our sample, we find a mean value of $\langle \Delta\sigma \rangle = 0.14 \pm 0.15$, or alternatively $\langle \sigma_{[\text{O III}]} / \sigma_* \rangle = 1.48 \pm 0.56$. This is very similar to the excess [O III] linewidth in higher-luminosity samples: Greene & Ho (2005) found $\langle \sigma_{[\text{O III}]} / \sigma_* \rangle = 1.43 \pm 0.75$ for Seyfert 2 galaxies overall in the MPA/JHU DR2 catalog with $\sigma_* > 70 \text{ km s}^{-1}$. On the other hand, the $\text{FWHM}_{[\text{O III}]}$ values do not reveal any strong excess linewidth for the core component. The mean value of ΔW for our sample is $\langle \Delta W \rangle = -0.05 \pm 0.12$, indicating that on average the [O III] FWHM values track the stellar velocity dispersion (albeit with substantial scatter), similar to results found by Nelson & Whittle (1996) for more massive Seyfert galaxies. The [S II] lines show a similar trend relative to the stellar velocity dispersions, with $\langle \Delta W_{[\text{S II}]} \rangle = -0.05 \pm 0.15$.

Overall, these results demonstrate that the relationships between [O III] linewidth and stellar velocity dispersion continue to hold for Seyfert 2 galaxies with stellar velocity dispersions of $\sim 40\text{--}80 \text{ km s}^{-1}$, and that the $\text{FWHM}_{[\text{O III}]}$ values are primarily driven by virial motion in the NLR. Nevertheless, the excess linewidth seen in the [O III] line wings, and in the $\sigma_{[\text{O III}]}$ values, indicates that even for these relatively low-luminosity, low-mass AGNs, nongravitational motion (presumably outflows driven by the central engine) does play a significant role in the NLR kinematics.

4.5. Polarization

The spectropolarimetry results for the wavelength region surrounding the $\text{H}\alpha$ emission line in the red-side spectra are shown in Figure 11. Each panel displays the total flux spectrum, the fractional polarization p given as the “rotated Stokes parameter” (Miller et al. 1988), and the Stokes flux, which is given by $p \times f_\lambda$. The clearest signature of a hidden broad line region would be a broad “bump” in the p spectrum at the $\text{H}\alpha$ emission line, which results in a Stokes flux spectrum resembling that of a Seyfert 1 galaxy (Antonucci & Miller 1985). Continuum polarization is another possible sign of a hidden active nucleus, but some care must be taken to distinguish it from polarization by transmission through aligned dust grains, either in the host galaxy or of Galactic origin.

In the continuum near $\text{H}\alpha$, the S/N in the total flux spectra

ranges from ~ 40 to 160 per pixel for these observations (Table 4). Since the spectra are strongly dominated by starlight, only relatively strong polarized broad lines ($p \gtrsim 1\text{--}2\%$ above the continuum level) could potentially be detected in observations of this quality, and none of these four objects exhibits any obvious polarization feature at $\text{H}\alpha$. The significance of any possible features in the Stokes q or u spectra was quantified using a method similar to that described by Barth et al. (1999). For each object, we fit quadratic polynomial models to the continuum in the red-side q and u spectra, excluding a $150\text{-}\text{\AA}$ wide region around $\text{H}\alpha$ from the fit. Over this $150\text{-}\text{\AA}$ wide region centered on $\text{H}\alpha$, the excess polarization in the q Stokes parameter relative to the continuum polarization is then $\delta_q = \langle q_{\text{data}} - q_{\text{model}} \rangle$. To evaluate the uncertainty on this measurement, we calculated the same quantity over a large number of randomly placed $150\text{-}\text{\AA}$ wide bins in the continuum regions of the spectrum over $5600\text{--}7600 \text{\AA}$. The standard deviation of these residual differences was taken to be the 1σ uncertainty ϵ_q for the measurement at $\text{H}\alpha$. This generally exceeds the error level from the propagated photon-counting statistics and detector readnoise because of small but unavoidable systematic errors in spectral extractions such as errors in interpolating fractional pixel values at the edges of the extraction apertures for spatially extended objects (Barth et al. 1999). These errors result in broad systematic wiggles in the p spectra, as seen in Figure 11. The significance of any polarization excess at $\text{H}\alpha$ relative to the fitted continuum level is then $\Delta_q = \delta_q / \epsilon_q$, and similarly for the u parameter. The measurements confirm that no significant $\text{H}\alpha$ line polarization is detected. The maximum deviation from the continuum polarization level is only at the 2σ level for the u Stokes parameter in SDSS 0947+5349. For all other objects the Stokes parameters at $\text{H}\alpha$ have $|\Delta_q| < 1$ and $|\Delta_u| < 1$.

The continuum polarization and polarization angle were measured over wavelength bins $4400\text{--}5500 \text{\AA}$ on the blue side and $6000\text{--}7500 \text{\AA}$ on the red side. All measurements were performed on the Stokes parameter spectra, with the results converted to p and θ as the final step. The results are reported in Table 4, along with the Galactic reddening $E(B-V)$ for these objects (Schlegel et al. 1998) and the maximum expected level of Galactic foreground polarization, $p_{\text{max}}(\%) = 9.0 \times E(B-V)$ (Serkowski et al. 1975). For the null standard HD 57702, we find blue and red-side polarizations of $(0.07 \pm 0.01)\%$ and $(0.08 \pm 0.01)\%$, respectively, so any systematic instrumental polarization should be at or below this level. The galaxies’ continuum polarizations are 0.2 to 0.76% , significantly larger than that of the null standard.

For three of the objects, the continuum polarization is only marginally higher (by $\lesssim 0.2\%$) than the maximum expected Galactic foreground polarization. The only object exhibiting a continuum polarization signal significantly above the Galactic foreground level is SDSS 1109+6123, which has $p = (0.76 \pm 0.10)\%$ and $(0.72 \pm 0.10)\%$ on the red and blue sides, respectively, while the Galactic foreground p_{max} along this sightline is only 0.1% . Thus, the detected polarization almost certainly arises within the host galaxy, but the limited S/N and lack of any polarized line features does not permit a clear interpretation of its physical origin. Electron scattering or dust scattering of a hidden AGN continuum could be responsible for the observed polarization. If the electron scattering mirror were located interior to the narrow-line region then the narrow emission lines should have a lower polarization than the surrounding continuum. This is not observed in

our data, but would be testable with higher S/N observations.

Polarization by transmission through foreground dust in the host galaxy is an alternative possibility, and is the dominant polarization mechanism in some low-luminosity AGNs with high internal extinction such as NGC 3718 (Barth et al. 1999). For SDSS 1109+6123, the Balmer decrement $H\alpha/H\beta$ is 2.94 ± 0.09 in the SDSS spectrum and 2.87 ± 0.10 in the LRISp spectrum, consistent with the Case B recombination value of 2.85 and smaller than the typical AGN narrow-line region value of ~ 3.1 (e.g., Osterbrock & Ferland 2006), so the reddening toward the NLR is too low to be determined accurately. If the dust transmission polarization within the host galaxy follows the Galactic relationship between reddening and maximum polarization, $p_{\max} = 9.0 \times E(B-V)$ (Serkowski et al. 1975), then the observed polarization would require $E(B-V) \gtrsim 0.08$ mag, much higher than the Galactic reddening of $E(B-V) = 0.011$ mag (Schlegel et al. 1998). For Case B recombination this reddening would modify the observed Balmer decrement to $H\alpha/H\beta \gtrsim 3.07$. Given the uncertainties on the measured Balmer decrements, we cannot fully rule out the possibility that the observed continuum polarization is dominated by dust transmission polarization within the host galaxy. Scattered light from a hidden AGN remains an intriguing possibility for this object, but very long spectropolarimetry exposures would be needed in order to achieve sufficient S/N to place interesting limits on the presence of polarized broad $H\alpha$ emission.

Nondetections of polarized emission lines or continuum in Seyfert 2 galaxies are unfortunately difficult to interpret; possible explanations include lack of a BLR, lack of a suitable scattering mirror, foreground dust absorption covering the host galaxy’s nucleus, or contamination by starlight that dilutes the strength of a scattered-light polarization signal. In starlight-dominated AGNs with hidden BLRs, the broad-line polarization is often $\lesssim 1\%$ above the continuum polarization (Barth et al. 1999; Moran et al. 2000), and the S/N of these observations is too low to detect such weak polarized line features.

4.6. Radio and X-ray Counterparts

We searched for counterparts to these sources in the online source catalogs of the FIRST (Becker et al. 1995) and NVSS (Condon et al. 1998) radio surveys, and the ROSAT All-Sky Survey (Voges et al. 1999). Only two objects were matched with sources in the radio catalogs: 1629+4254 is detected in the FIRST survey with $f_\nu = 1.79$ mJy, and 1032+6502 is an NVSS source with a flux density of 7.6 mJy.

The only two objects in this sample detected in the ROSAT All-Sky Survey are the two previously known AGNs with weak broad $H\alpha$ emission, 1032+6502 and 1440+0247. In both cases, the association with the ROSAT source has previously been noted: 1032+6502 (Boller et al. 1992; Moran et al. 1996) with a soft X-ray flux of 6.2×10^{-13} ergs cm^{-2} s^{-1} , and 1440+0247 with a flux of 2.8×10^{-13} ergs cm^{-2} s^{-1} in the ROSAT 0.1–2.4 keV band (Anderson et al. 2003).

The lack of additional radio and X-ray detections for other objects in this sample is not surprising. Among the Type 1 objects found by GH04, only one was detected in deep VLA imaging at 6 cm, and the entire GH04 sample is extremely radio quiet (Greene et al. 2006). Similarly, the GH04 sample is faint in X-rays, with only 30% of the objects detected in the ROSAT All-Sky Survey. If the Type 2 objects in our sample are intrinsically similar objects with hidden broad-line regions that are obscured either by a compact torus or by larger-

scale dust lanes in the host galaxy, the soft X-ray flux would likely be strongly attenuated as well. Deep *XMM-Newton* observations of a few objects in this sample have recently been obtained in order to search for nuclear X-ray sources and to constrain the amount of obscuring material toward the nuclei; the results of these observations will be presented in a forthcoming paper.

4.7. Host Galaxy Morphologies and Stellar Populations

The host galaxies of AGNs with low-mass black holes exhibit a surprising range of morphologies. NGC 4395 is an essentially bulgeless, late-type Sd spiral (Filippenko & Sargent 1989), and serves as the best demonstration that black holes can form in some galaxies that lack a substantial central bulge. On the other hand, the structure of POX 52 is best described as a dwarf elliptical (Barth et al. 2004; Thornton et al. 2008), although with a host galaxy absolute magnitude of $M_V = -17.6$ and Sérsic index of ~ 4 it is both more luminous and more centrally concentrated than typical dE galaxies (Binggeli & Jerjen 1998). All of the host galaxies in the GH04 Seyfert 1 sample are more luminous than these two nearby objects, but analysis of *HST* images shows that they also exhibit a range of morphologies, with about 60% being disk dominated galaxies that contain a bulge or pseudobulge, and the remainder being compact galaxies with spheroidal morphologies similar to POX 52 (Greene, Ho, & Barth 2008).

From examination of the SDSS images for this sample, about half of the objects appear to have definite or likely disks, while the remaining objects appear compact without obvious disks. These may be objects with POX 52-type host galaxies, but higher-resolution imaging would be needed to determine the morphological types. The SDSS concentration index C , defined as the ratio of the radii containing 90% and 50% of the total galaxy light in the r band, gives a rough quantitative measure of morphology (Strateva et al. 2001), as there is a general separation between early-type, bulge-dominated galaxies with $C \gtrsim 2.6$ and late-type, disk-dominated galaxies with $C < 2.6$. The concentration values for our sample, taken from the MPA/JHU catalog and SDSS archives, are listed in Table 1. The median concentration for our sample is 2.59, only slightly lower than the median concentration for the full AGN sample in the DR2 MPA/JHU catalog overall, and the distribution of concentration values is consistent with a mixed population including some elliptical or spheroidal hosts. Figure 12 shows a color-magnitude diagram for the sample, using the extinction-corrected and k -corrected SDSS photometric data in the g and r bands, and compared with standard galaxy colors from Fukugita et al. (1995). The hosts span a wide range in color, corresponding to typical colors ranging from those of ellipticals to late-type spirals, with all but one object having $g-r$ between 0.4 and 0.8.

Only one galaxy in this sample, 1109+6123, appears to be a promising candidate for a very late-type, nearly bulgeless (\sim Sd) disk galaxy similar to NGC 4395 (see §4.10). This late-type disk galaxy is a notable outlier in this sample, both in terms of its low luminosity ($M_g = -16.8$ mag) and its blue color ($g-r = 0.28$ mag). Even with SDSS, there are remarkably few known examples of Seyfert nuclei in very late-type, low-mass disk galaxies. The small number of NGC 4395 analogs in SDSS is largely a selection effect: galaxies of this low luminosity are only sampled in the SDSS spectroscopic survey out to $z \approx 0.02-0.03$ due to the apparent magnitude limit of $r = 17.77$ of the spectroscopic survey. Since SDSS probes only a very small volume for these NGC 4395-type

objects, our sample is biased toward somewhat more luminous host galaxies and more luminous AGNs.

Some limited information on stellar populations and star formation history can be obtained from the $D_n(4000)$ and $H\delta_A$ indices in the MPA/JHU catalog. The measurement of these parameters is described in detail by Kauffmann et al. (2003a). The $D_n(4000)$ index measures the strength of the 4000 Å break, which increases monotonically with population age for a single-burst population. The $H\delta_A$ index is a measure of the $H\delta$ absorption-line strength, which, for a single-burst population, is strongest for ages of $\sim 0.1 - 1$ Gyr. Kauffmann et al. (2003a) showed that population synthesis models for galaxies incorporating exponentially declining star formation rates and random bursts of star formation were generally able to track the locus of SDSS galaxies in a plot of $H\delta_A$ vs. $D_n(4000)$. To illustrate the range of stellar population ages in our sample, Figure 13 displays the values of $H\delta_A$ and $D_n(4000)$ from the MPA/JHU catalogs for our sample, in comparison with the overall sample of all galaxies in the catalog having $\log(M_*/M_\odot) < 10$. The AGN hosts exhibit a wide range in both stellar indices, but avoid the largest values of $D_n(4000)$ (corresponding to the oldest stellar populations). In this respect, they follow the same general trends as the overall population of Seyfert 2 galaxies in SDSS, as shown by Kewley et al. (2006): the Seyfert 2s tend to be found in hosts with $D_n(4000)$ in the range $\sim 1.2 - 1.8$, while LINERs are found in systematically older host galaxies with $D_n(4000)$ up to ~ 2.2 (Kewley et al. 2006).

4.8. Black Hole Mass and Eddington Ratio

For Seyfert 2 galaxies, there is no direct way to measure the black hole mass from the optical spectrum of the AGN, and the best available alternative is to use the stellar velocity dispersion and the $M_{\text{BH}} - \sigma_*$ relationship to obtain a rough estimate of M_{BH} . As shown by Barth et al. (2005), the low-mass Seyfert 1 galaxies from GH04 lie fairly close to the extrapolated $M_{\text{BH}} - \sigma_*$ relation, on average having slightly higher black hole masses than would be predicted from their velocity dispersions. The mean offset between the estimated black hole masses for these galaxies and the Tremaine et al. (2002) $M_{\text{BH}} - \sigma_*$ relation is 0.23 dex. This offset is likely to reflect a flattening in the slope of the $M_{\text{BH}} - \sigma_*$ relation at low masses (Wyithe 2006; Greene & Ho 2006), but, lacking a more detailed direct measurement of the change in the $M_{\text{BH}} - \sigma_*$ slope as a function of σ_* , we simply assume a uniform offset. Since the Seyfert 2 galaxies in this sample fall in the same range of stellar velocity dispersions as the GH04 Seyfert 1 galaxies, we use the σ_* measurements to estimate M_{BH} , assuming an offset of 0.23 dex relative to the Tremaine et al. $M_{\text{BH}} - \sigma_*$ relation. For the objects not having direct measurements of σ_* , we use $\text{FWHM}_{[\text{O III}]}/2.35$ in place of σ_* to estimate M_{BH} . With this prescription, the black hole mass estimates for this sample are in the range $4.7 < \log(M_{\text{BH}}/M_\odot) < 6.8$, with a median value of $\log(M_{\text{BH}}/M_\odot) = 6.1$. The uncertainty in any individual mass estimate is likely to be at least 0.3 dex, however, due to the scatter in the $M_{\text{BH}} - \sigma_*$ relation and the poorly constrained $M_{\text{BH}} - \sigma_*$ slope at low masses.

Similarly, the bolometric luminosities can only be estimated indirectly. The best available indicator of the AGN luminosity in these objects is the [O III] $\lambda 5007$ luminosity, which we assume to arise predominantly from the AGN rather than from star-forming regions, based on the locations of these galaxies in the BPT diagnostic diagrams. (As a caveat, we note that for host galaxies of relatively low metallicity,

the contribution from star-forming regions to the [O III] luminosity could be greater than in high-metallicity galaxies, but we have no direct diagnostics of the star-formation rate in the nuclei.) From a sample of low-redshift Seyfert 1 galaxies and quasars, Heckman et al. (2004) found an [O III] bolometric correction of $L_{\text{bol}}/L_{[\text{O III}]} \approx 3500$, with a typical scatter of 0.38 dex. We adopt this prescription for our sample, but note as an additional caveat that there is evidence that the $L_{[\text{O III}]} / L_X$ ratio decreases systematically with AGN luminosity (Netzer et al. 2006), implying that there is a luminosity dependence to the [O III] bolometric correction. The [O III] luminosities for our sample are listed in Table 1; most are in the range $6.0 < \log(L_{[\text{O III}]} / L_\odot) < 7.5$, implying bolometric luminosities of $43 < \log[L_{\text{bol}} / (\text{ergs s}^{-1})] < 44.6$ for most objects. The two very low-redshift galaxies with late-type spiral hosts, 1032+6502 and 1109+6123, are much lower in luminosity, both having $\log(L_{[\text{O III}]} / L_\odot) \approx 4.9$ and $L_{\text{bol}} \approx 10^{42}$ ergs s^{-1} .

Combining the black hole masses and luminosities, we can obtain rough estimates of $L_{\text{bol}}/L_{\text{Edd}}$. The distribution of $L_{\text{bol}}/L_{\text{Edd}}$ estimates is shown in Figure 14; the median value of $\log(L_{\text{bol}}/L_{\text{Edd}})$ for the sample is -0.4 . Although these values of $L_{\text{bol}}/L_{\text{Edd}}$ will be extremely uncertain for individual galaxies, the estimates suggest that many of these galaxies contain black holes that are undergoing a significant episode of accretion. Greene & Ho (2007) found that in their DR4 sample of Seyfert 1 galaxies with $M_{\text{BH}} < 2 \times 10^6 M_\odot$, the distribution of Eddington ratio is peaked at $\log(L_{\text{bol}}/L_{\text{Edd}}) \approx -0.5$, highlighting the similarities between the two samples.

Alternatively, assuming the same [O III] bolometric correction, we can estimate the minimum black hole mass that would be required to support the luminosity in each object if all objects are radiating at $L_{\text{bol}}/L_{\text{Edd}} < 1$. Figure 15 shows the resulting lower limits to M_{BH} as a function of σ_* (again using $\text{FWHM}_{[\text{O III}]}/2.35$ in place of σ_* for the two objects without measured velocity dispersions). The minimum required black hole masses for the sample are generally low, and 2/3 of the galaxies have $M_{\text{BH}}(\text{min}) < 10^6 M_\odot$. The results are consistent with most objects having black hole masses that fall close to or below the low-mass extrapolation of the $M_{\text{BH}} - \sigma_*$ relation from Tremaine et al. (2002); eight galaxies in the sample have minimum M_{BH} values that lie above the $M_{\text{BH}} - \sigma_*$ relation. The largest deviation above the extrapolated $M_{\text{BH}} - \sigma_*$ relation is found for 1440+0247, which lies approximately an order of magnitude higher than the Tremaine et al. $M_{\text{BH}} - \sigma_*$ relation extrapolated to $\sigma_* = 45 \text{ km s}^{-1}$. Given the substantial uncertainties in the [O III] bolometric correction, these lower limits to M_{BH} should be viewed cautiously on a case-by-case basis, but on the whole these results are consistent with expectations for a sample of black holes of relatively low mass in which many of the black holes are undergoing a significant accretion episode.

4.9. Unified Models and the Obscuring Torus

These Seyfert 2 galaxies and the GH04 Seyfert 1 objects do not constitute perfectly matched samples in terms of their nuclear or host galaxy properties, as a result of the very different selection criteria that were used for the two samples. Nevertheless, the two samples do occupy similar and overlapping ranges in some key parameters. As shown in Figure 16, the distributions of g -band absolute magnitudes are overlapping but not identical; the Seyfert 2s were selected based on an absolute magnitude cut and all have $M_g \geq -19.7$ mag, while the GH04 objects were selected without regard to host

galaxy properties, and their distribution extends to slightly more luminous galaxies, up to $M_g = -20.6$. The GH04 sample also does not contain any host galaxies as faint as the least luminous Seyfert 2 galaxy in this sample, 1109+6123, with $M_g = -16.8$. In terms of [O III] luminosity, which is the best available indicator of total AGN luminosity, the two samples occupy overlapping ranges with most galaxies in the range $L_{[\text{O III}]} \sim 10^6 - 10^8 L_\odot$; again, the Type 1 sample extends to slightly higher luminosities and the Type 2 sample extends to lower luminosities, with the galaxy 1109+6123 falling at the low-luminosity end of the distribution.

Although the narrow-line ratios of the two samples occupy overlapping ranges, as seen in Figure 5, there are some key differences between the Type 1 and Type 2 objects. From inspection of Figure 5, it is evident that the Seyfert 2 galaxies from this sample have somewhat lower values of [O III]/H β on average than the GH04 sample. The median values of [O III]/H β are 7.9 and 4.9 for the Type 1 and Type 2 samples respectively, and a Kolmogorov-Smirnov (K-S) test confirms that the two distributions are significantly different, with a 1.4% probability of being drawn from the same parent population. We also examine the [O II] λ 3727/[O III] λ 5007 ratio for the two samples, measured from the SDSS spectra since the ESI spectra do not cover [O II] λ 3727 for most objects (see Figure 16). The Type 1 and Type 2 objects have median values for [O II]/[O III] of 0.23 and 0.61, respectively. A K-S test shows that the two distributions of [O II]/[O III] have only a 3×10^{-5} probability of being drawn from the same parent population.

The higher [O II]/[O III] ratio in the Type 2 objects is intriguing in light of similar trends found recently among high-luminosity AGNs. Ho (2005) showed that among the PG quasar sample, the [O II]/[O III] ratio is generally consistent with that expected from AGN photoionization, with no evidence for an additional contribution to the [O II] emission from star-forming regions. Following up on this study, Kim et al. (2006) found that luminous Type 2 AGNs from SDSS such as those found by Zakamska et al. (2003) have enhanced levels of [O II] emission relative to what is seen in a corresponding Type 1 AGN sample from SDSS, possibly indicating an elevated rate of star formation in the Type 2 objects compared to the Type 1 objects. This observation presents a strong challenge to the simplest unified models, in which Type 1 and Type 2 AGNs differ only by orientation and obscuration of the central engine. The low-mass Seyfert 2 hosts evidently follow the same trend of enhanced [O II] emission: the median values of $\log([\text{O III}]/\text{H}\beta)$ and $\log([\text{O II}]/[\text{O III}])$ for the Type 2 objects in this sample are 0.69 and -0.21 , respectively, which fall remarkably close to the values for these line ratios measured from the composite Type 2 quasar spectrum of Zakamska et al. (2003), as displayed in Figure 7 of Kim et al. (2006). The lower [O III]/H β ratios among the Seyfert 2 sample could be another manifestation of a larger contribution of star-forming regions to the spectra, although another possibility is that the Seyfert 2 galaxies have slightly lower NLR ionization parameter than the GH04 Seyfert 1 galaxies.

Aside from the question of the relative amounts of star formation in the Type 1 and Type 2 samples, the more fundamental unification question remains: do they all have intrinsically similar central engines, in which case the presence or absence of broad emission lines would depend primarily on their orientation and the degree of obscuration along our line of sight? Or, alternatively, are some of the Type 2 objects “true” Type 2 AGNs that intrinsically lack a BLR? There is growing obser-

vational evidence that at low luminosities, there is a population of Seyfert 2 galaxies that do not exhibit polarized broad-line emission or X-ray absorption (e.g. Pappa et al. 2001; Tran 2003; Nicastro et al. 2003; Bianchi et al. 2008), suggesting that the line of sight to the nucleus is unobscured and the BLR is not present. One scenario to explain true Seyfert 2 nuclei has been proposed by Nicastro (2000); in this model, the BLR consists of an accretion disk wind and when $L_{\text{bol}}/L_{\text{Edd}}$ falls below a critical value of $\sim 10^{-3}$, the luminosity is insufficient for the disk to form a radiation-pressure dominated region from which to launch the wind. In another model proposed by Laor (2003), there is a maximum BLR linewidth of $\sim 25,000 \text{ km s}^{-1}$ above which the BLR clouds do not survive, and there is a critical luminosity below which the BLR radius shrinks to a size where the corresponding Keplerian velocities exceed this maximum linewidth. At present it is not completely clear whether L_{bol} or $L_{\text{bol}}/L_{\text{Edd}}$ is the primary parameter that determines whether a BLR forms (or whether there may be some additional key parameter), and further exploration of the properties of the least luminous Seyfert 2 galaxies is needed in order to resolve this question. As described above, most of our sample consists of objects with relatively high $L_{\text{bol}}/L_{\text{Edd}}$, and with L_{bol} in the range $10^{43} - 10^{44.6} \text{ ergs s}^{-1}$; in both the Nicastro (2000) and Laor (2003) scenarios these objects would be above the critical luminosity or Eddington ratio needed to support BLRs.

A closely related question is the nature of the obscuring torus in unified models of AGNs and whether the properties or existence of the torus depends on AGN luminosity or other properties. One attractive possibility for the origin of the obscuring torus is that it may be the dusty component of a wind driven from the surface of the accretion disk (e.g., Konigl & Kartje 1994). Elitzur & Shlosman (2006) have recently examined the dynamics of hydromagnetic disk winds and the dependence of outflow properties on the AGN luminosity. A key prediction of their model is that for AGN luminosities below $\sim 10^{42} \text{ ergs s}^{-1}$, the AGN is not powerful enough to sustain the torus wind, and the torus should therefore not be present in very low-luminosity AGNs. While most of our sample is more luminous than this threshold, the least luminous object in our sample (1109+6123) presents a particularly interesting test case. Its narrow-line spectrum and host galaxy are nearly identical to NGC 4395 (§4.10), and it is the best Type 2 counterpart to NGC 4395 known. NGC 4395 has a bolometric luminosity of $\sim 5 \times 10^{40} \text{ ergs s}^{-1}$ (Moran et al. 1999; Peterson et al. 2005), more than an order of magnitude below the typical cutoff luminosity for a wind-driven torus in the Elitzur & Shlosman model. While the bolometric luminosity of SDSS 1109+6123 is unknown, its [O III] luminosity is about 40% smaller than that of NGC 4395.

This galaxy and NGC 4395 together pose an interesting challenge to models for the obscuring torus: *the Type 1/Type 2 dichotomy apparently extends down to the very lowest luminosities seen among nearby Seyfert galaxies*, below $L_{\text{bol}} = 10^{41} \text{ ergs s}^{-1}$. While this is already well established for massive host galaxies (Ho 2008), the discovery of a near-perfect Type 2 analog to NGC 4395 raises the possibility that the obscuring torus might still be present even at these very low masses and luminosities. The detection of continuum polarization in 1109+6123 gives an intriguing hint of an obscured nucleus, and further searches for the presence of an obscuring torus and obscured BLR in 1109+6123, including deeper spectropolarimetry, X-ray observations, and mid-infrared spectroscopy, may provide critical new tests for

wind-driven torus models. Alternatively, 1109+6123 might be a “true” Seyfert 2 that intrinsically lacks a BLR. In this situation, the question remains: why would a BLR occur in NGC 4395, but not in 1109+6123, which has a similar [O III] luminosity, and presumably a similar black hole mass as well? If 1109+6123 is a true unobscured Seyfert 2, this would imply that the formation or lack of a BLR must depend on some other properties of the AGN in addition to L_{bol} or $L_{\text{bol}}/L_{\text{Edd}}$.

Obscuration by larger-scale dust lanes within the host galaxies is likely to play some role as well in determining the relative numbers of Type 1 and Type 2 AGNs in low-mass disk galaxies. The SDSS images show that three objects in our sample are nearly edge-on disk galaxies, in which host galaxy-scale obscuration could easily explain the lack of broad emission lines in the optical spectrum. In contrast, in the GH04 Seyfert 1 sample, none of the spiral host galaxies are close to edge-on (Greene, Ho, & Barth 2008). This is consistent with trends seen in the general Seyfert population; Seyfert 1 nuclei are deficient in edge-on host galaxies relative to face-on hosts (Keel 1980; Maiolino & Rieke 1995). Similarly, in deep X-ray surveys, the difference between “optically dull” X-ray sources and broad-lined AGNs can be attributed at least in part to host galaxy-scale obscuration related to host inclination (Rigby et al. 2006). A search for nuclear dust lanes in high-resolution images would provide some constraints on the impact of host-galaxy scale obscuring material (e.g., Malkan et al. 1998).

4.10. Notes on Individual Objects

0110+0026: This galaxy was selected from the MPA/JHU SDSS catalog of narrow-line AGNs, but it has a very prominent broad $H\alpha$ emission line visible in both the SDSS and ESI spectra.

0914+0238: A possible companion is located about $25''$ to the east of this galaxy, but its redshift is unknown (not cataloged in NED).

0947+5349: This galaxy appears to be part of an interacting triplet, labeled in NED as CGCG 265–039. The redshifts of the two larger galaxies just south of it in the SDSS image are unknown.

1032+6502: Also known as NGC 3259, this is a nearby SBbc galaxy. It was previously identified as a ROSAT source by Boller et al. (1992) and Moran et al. (1996), and as a Seyfert by Hao et al. (2005a) from the SDSS spectrum. Our Keck spectrum confirms the presence of a weak broad $H\alpha$ emission line. Multicolor *HST* images show that it has a substantial bulge, with $M \approx 3 \times 10^8 M_{\odot}$ and a predominantly old stellar population (Carollo et al. 2007). It was also recently noted as an example of a galaxy containing both a nuclear star cluster and an AGN by Seth et al. (2008).

1109+6123: Also known as UGC 06192 or MCG +10-16-069, this galaxy was not previously identified as hosting an AGN prior to SDSS. It has an unusual high-excitation narrow-line spectrum with the lowest [N II]/ $H\alpha$ ratio among our sample ([N II]/ $H\alpha$ = 0.18), characteristic of low-metallicity AGNs and very similar to the spectrum of NGC 4395 (Kraemer et al. 1999), but without any hint of broad emission lines. Its [O III] luminosity, from the MPA/JHU catalog, is $\log(L_{[\text{O III}]}/L_{\odot}) = 4.94$. This is very similar to the narrow-line luminosity of NGC 4395, which has $\log(L_{[\text{O III}]}/L_{\odot}) = 5.09$ based on the emission-line data from Kraemer et al. (1999) and a distance of 4.3 Mpc (Thim et al. 2004). With $\log(M_{*}/M_{\odot}) = 8.07$, this galaxy has the lowest stellar mass of any unambiguous Seyfert 2 galaxy in either the DR2 or DR4 MPA/JHU AGN catalogs.

From examination of the SDSS images, the host galaxy is a low surface brightness, late-type spiral, probably best classified as Scd or Sd. A surface brightness profile measured from the SDSS *i*-band image reveals that the host galaxy is well described by an exponential disk with a scale length of $7''.9$ (≈ 1.1 kpc), with a slight central excess over the exponential profile in the inner $\sim 5''$ that may indicate the presence of a small bulge or pseudobulge. Overall, the properties of this galaxy make it a near-twin of NGC 4395, aside from the lack of broad emission lines in its spectrum. Deeper and higher-resolution imaging with *HST* would be particularly valuable to definitively detect or constrain the presence of a bulge in this galaxy and to determine whether a compact central star cluster is present.

1432+0046: The SDSS image shows an apparent close companion just to the east of this galaxy, but it is a chance projection; the disk galaxy is SDSS J143232.24+004617.4, at $z = 0.034$.

1440+0247: Also known as Tol 1437+030, this object was identified as an AGN by Bohuski et al. (1978). It has also been noted as an AGN from the SDSS spectrum by Anderson et al. (2003), Kniazev et al. (2004), and Hao et al. (2005a). Its spectrum is very similar to those of NGC 4395 and POX 52 in terms of the narrow-line ratios as well as the detection of high-ionization lines (up to [Fe X] and [Fe XI]), but broad $H\alpha$ emission is only marginally detectable in the ESI spectrum.

1629+4254: At first glance this appears to be a likely Seyfert 1 galaxy because of the broad base to the $H\alpha$ +[N II] emission blend, but our line profile fits show that the broad bases are present on all of the forbidden lines. The [O III] profile has an extraordinary broad and redshifted component (FWHM = 589 km s^{-1} , $\Delta v = +223 \text{ km s}^{-1}$ relative to the core component), while the core component is fairly narrow (FWHM = $78 \pm 1 \text{ km s}^{-1}$). From the FIRST radio detection, the radio power of this source at 20 cm is $5 \times 10^{21} \text{ W Hz}^{-1}$. Multicomponent [O III] profiles are often found in objects with linear radio sources (Whittle et al. 1988), and the detection of a radio counterpart in the FIRST survey makes this an unusual object relative to the very radio-quiet GH04 sample. To compare with the radio properties of the GH04 objects, we follow Greene et al. (2006) and adopt the radio loudness parameter $R = f_{6 \text{ cm}}/f_{4400}$. We estimate the flux density of the (presumably obscured) optical nonstellar continuum by using the [O III] flux as a proxy, assuming the median ratio of [O III] luminosity to 4400 Å continuum luminosity for the GH04 sample (Greene et al. 2006). This yields $f(4400 \text{ Å}) \approx 0.6 \text{ mJy}$. Based on the FIRST 20 cm flux and an assumed flat spectral index between 6 and 20 cm, which is typical of low-luminosity Seyfert 2 galaxies (Ulvestad & Ho 2001), we find $R \approx 3$. This is formally in the radio-quiet regime (since $R < 10$), but this value of R is greater than most of the upper limits found for the GH04 sample (Greene et al. 2006).

5. SUMMARY AND CONCLUSIONS

We have presented an initial, exploratory study of the properties of Seyfert 2 galaxies with sub- L^* luminosities selected from the Sloan Digital Sky Survey. Our measurements reveal very low central stellar velocity dispersions ($\sigma_{*} < 60 \text{ km s}^{-1}$) in 12 objects; these are among the smallest velocity dispersions found in any AGN host galaxies, and imply that these galaxies contain some of the least massive black holes in any known AGNs. We have also identified one of the very few known examples of a high-excitation Seyfert 2 nucleus in a late-type, dwarf spiral host galaxy similar to NGC 4395.

The correlations between [O III] linewidth and σ_* established for higher-mass Seyferts continue to hold in this low-mass regime, while the low-mass Seyfert 2 galaxies exhibit an unusually high incidence of peculiarities (such as redward asymmetries and double-peaked profiles) in their forbidden emission lines. Using rough estimates of black hole mass and bolometric luminosity, we find that the median value of $L_{\text{bol}}/L_{\text{Edd}}$ for this sample is 0.4, indicating that many of these are objects in which the black hole is undergoing a major growth phase. Future work on these objects will include *XMM-Newton* observations and *Spitzer* mid-infrared spectroscopy, in order to search for evidence of nuclear obscuration and to test whether the obscuring torus of AGN unified models is present in this low-mass, low-luminosity regime.

We are very grateful to Guinevere Kauffmann and her collaborators for making their AGN and stellar mass catalogs available to the community. We thank George Djorgovski for obtaining some preliminary ESI spectra for this project, Craig Markwardt and Mike Blanton for their excellent and

useful IDL software, Michael Strauss for providing plotting scripts, and an anonymous referee for suggestions that improved the manuscript. Research by A.J.B. was supported by the UC Irvine Physical Sciences Innovation Fund and by NSF grant AST-0548198. Data presented herein were obtained at the W.M. Keck Observatory, which is operated as a scientific partnership among Caltech, the University of California, and NASA. The Observatory was made possible by the generous financial support of the W.M. Keck Foundation. The authors wish to recognize and acknowledge the very significant cultural role and reverence that the summit of Mauna Kea has always had within the indigenous Hawaiian community. Funding for the SDSS and SDSS-II has been provided by the Alfred P. Sloan Foundation, the Participating Institutions, the National Science Foundation, the U.S. Department of Energy, the National Aeronautics and Space Administration, the Japanese Monbukagakusho, the Max Planck Society, and the Higher Education Funding Council for England. The SDSS Web Site is <http://www.sdss.org/>.

REFERENCES

- Abazajian, K., et al. 2004, *AJ*, 128, 502
 Anderson, S. F., et al. 2003, *AJ*, 126, 2209
 Antonucci, R. R. J., & Miller, J. S. 1985, *ApJ*, 297, 621
 Baldwin, J. A., Phillips, M. M., & Terlevich, R. 1981, *PASP*, 93, 5
 Barth, A. J., Filippenko, A. V., & Moran, E. C. 1999, *ApJ*, 525, 673
 Barth, A. J., Greene, J. E., & Ho, L. C. 2005, *ApJ*, 619, L151
 Barth, A. J., Ho, L. C., Rutledge, R. E., & Sargent, W. L. W. 2004, *ApJ*, 607, 90
 Barth, A. J., Ho, L. C., & Sargent, W. L. W. 2002, *AJ*, 124, 2607
 Becker, R. H., White, R. L., & Helfand, D. J. 1995, *ApJ*, 450, 559
 Bian, W., & Zhao, Y. 2004, *MNRAS*, 347, 607
 Bian, W., Yuan, Q., & Zhao, Y. 2006, *MNRAS*, 367, 860
 Bianchi, S., Corral, A., Panessa, F., Barcons, X., Matt, G., Bassani, L., Carrera, F. J., & Jiménez-Bailón, E. 2008, *MNRAS*, 108
 Binggeli, B., & Jerjen, H. 1998, *A&A*, 333, 17
 Blanton, M. R., & Roweis, S. 2007, *AJ*, 133, 734
 Bohuski, T. J., Fairall, A. P., & Weedman, D. W. 1978, *ApJ*, 221, 776
 Boller, T., Meurs, E. J. A., Brinkmann, W., Fink, H., Zimmermann, U., & Adorf, H.-M. 1992, *A&A*, 261, 57
 Carollo, C. M., Scarlata, C., Stiavelli, M., Wyse, R. F. G., & Mayer, L. 2007, *ApJ*, 658, 960
 Clemens, D. P., & Tapia, S. 1990, *PASP*, 102, 179
 Condon, J. J., Cotton, W. D., Greisen, E. W., Yin, Q. F., Perley, R. A., Taylor, G. B., & Broderick, J. J. 1998, *AJ*, 115, 1693
 Dong, X., et al. 2007, *ApJ*, 657, 700
 Elizur, M., & Shlosman, I. 2006, *ApJ*, 648, L101
 Ferrarese, L., & Merritt, D. 2000, *ApJ*, 539, L9
 Ferrarese, L., Pogge, R. W., Peterson, B. M., Merritt, D., Wandel, A., & Joseph, C. L. 2001, *ApJ*, 555, L79
 Filippenko, A. V., & Ho, L. C. 2003, *ApJ*, 588, L13
 Filippenko, A. V., & Sargent, W. L. W. 1989, *ApJ*, 342, L11
 Fukugita, M., Shimasaku, K., & Ichikawa, T. 1995, *PASP*, 107, 945
 Gebhardt, K., et al. 2000, *ApJ*, 539, L13
 Gebhardt, K., et al. 2001, *AJ*, 122, 2469
 Goodrich, R. W., Cohen, M. H., & Putney, A. 1995, *PASP*, 107, 179
 Greene, J. E., & Ho, L. C. 2004, *ApJ*, 610, 622 (GH)
 Greene, J. E., & Ho, L. C. 2005, *ApJ*, 627, 721
 Greene, J. E., & Ho, L. C. 2006, *ApJ*, 641, L21
 Greene, J. E., Ho, L. C., & Ulvestad, J. S. 2006, *ApJ*, 636, 56
 Greene, J. E., Ho, L. C., & Barth, A. J. 2008, *ApJ*, submitted
 Greene, J. E., & Ho, L. C. 2007, *ApJ*, 670, 92
 Groves, B. A., Heckman, T. M., & Kauffmann, G. 2006, *MNRAS*, 371, 1559
 Grupe, D., & Mathur, S. 2004, *ApJ*, 606, L41
 Hao, L., et al. 2005a, *AJ*, 129, 1783
 Hao, L., et al. 2005b, *AJ*, 129, 1795
 Heckman, T. M., Miley, G. K., van Brugel, W. J. M., & Butcher, H. R. 1981, *ApJ*, 247, 403
 Heckman, T. M., Kauffmann, G., Brinchmann, J., Charlot, S., Tremonti, C., & White, S. D. M. 2004, *ApJ*, 613, 109
 Ho, L. C. 2008, *ARA&A*, in press
 Ho, L. C., Filippenko, A. V., & Sargent, W. L. W. 1997, *ApJS*, 112, 315
 Ho, L. C. 2005, *ApJ*, 629, 680
 Kauffmann, G., et al. 2003a, *MNRAS*, 341, 33
 Kauffmann, G., et al. 2003b, *MNRAS*, 346, 1055
 Keel, W. C. 1980, *AJ*, 85, 198
 Kewley, L. J., Heisler, C. A., Dopita, M. A., & Lumsden, S. 2001, *ApJS*, 132, 37
 Kewley, L. J., Groves, B., Kauffmann, G., & Heckman, T. 2006, *MNRAS*, 372, 961
 Kim, M., Ho, L. C., & Im, M. 2006, *ApJ*, 642, 702
 Kniazev, A. Y., Pustilnik, S. A., Grebel, E. K., Lee, H., & Pramskij, A. G. 2004, *ApJS*, 153, 429
 Konigl, A., & Kartje, J. F. 1994, *ApJ*, 434, 446
 Kormendy, J., & Richstone, D. 1995, *ARA&A*, 33, 581
 Kraemer, S. B., Ho, L. C., Crenshaw, D. M., Shields, J. C., & Filippenko, A. V. 1999, *ApJ*, 520, 564
 Kunth, D., Sargent, W. L. W., & Bothun, G. D. 1987, *AJ*, 93, 29
 Laor, A. 2003, *ApJ*, 590, 86
 Leonard, D. C., Filippenko, A. V., Chornock, R., & Foley, R. J. 2002, *PASP*, 114, 1333
 Maiolino, R., & Rieke, G. H. 1995, *ApJ*, 454, 95
 Malkan, M. A., Gorjian, V., & Tam, R. 1998, *ApJS*, 117, 25
 Mathewson, D. S., & Ford, V. L. 1970, *MNRAS*, 74, 139
 Merritt, D., Ferrarese, L., & Joseph, C. L. 2001, *Science*, 293, 1116
 Miller, J. S., Robinson, L. B., & Goodrich, R. W. 1988, *Instrumentation for Ground-Based Optical Astronomy, Present and Future*, ed. L.B. Robinson (New York: Springer-Verlag), 157
 Moran, E. C., Halpern, J. P., & Helfand, D. J. 1996, *ApJS*, 106, 341
 Moran, E. C., Filippenko, A. V., Ho, L. C., Shields, J. C., Belloni, T., Comastri, A., Snowden, S. L., & Sramek, R. A. 1999, *PASP*, 111, 801
 Moran, E. C., Barth, A. J., Kay, L. E., & Filippenko, A. V. 2000, *ApJ*, 540, L73
 Nelson, C. H., & Whittle, M. 1996, *ApJ*, 465, 96
 Netzer, H., Maimieri, V., Rosati, P., & Trakhtenbrot, B. 2006, *A&A*, 453, 525
 Nicastro, F. 2000, *ApJ*, 530, L65
 Nicastro, F., Martocchia, A., & Matt, G. 2003, *ApJ*, 589, L13
 Osterbrock, D. E., & Ferland, G. J. 2006, *Astrophysics of Gaseous Nebulae and Active Galactic Nuclei*, 2nd. ed. (Sausalito, CA: University Science Books)
 Osterbrock, D. E., & Mathews, W. G. 1986, *ARA&A*, 24, 171
 Pappa, A., Georgantopoulos, I., Stewart, G. C., & Zezas, A. L. 2001, *MNRAS*, 326, 995
 Peterson, B. M., et al. 2005, *ApJ*, 632, 799
 Rigby, J. R., Rieke, G. H., Donley, J. L., Alonso-Herrero, A., & Pérez-González, P. G. 2006, *ApJ*, 645, 115
 Salvander, S., Shields, G. A., Gebhardt, K., & Bonning, E. W. 2007, *ApJ*, 662, 131
 Satyapal, S., Vega, D., Heckman, T., O'Halloran, B., & Dudik, R. 2007, *ApJ*, 663, L9
 Schlegel, D. J., Finkbeiner, D. P., & Davis, M. 1998, *ApJ*, 500, 525

- Serkowski, K., Mathewson, D. L., & Ford, V. L. 1975, *ApJ*, 196, 261
- Seth, A., Agueros, M., Lee, D., & Basu-Zych, A. 2008, *ApJ*, in press (arXiv:0801.0439)
- Sheinis, A. I., Bolte, M., Epps, H. W., Kibrick, R. I., Miller, J. S., Radovan, M. V., Bigelow, B. C., & Sutin, B. M. 2002, *PASP*, 114, 851
- Shields, G. A., Gebhardt, K., Salviander, S., Wills, B. J., Xie, B., Brotherton, M. S., Yuan, J., & Dietrich, M. 2003, *ApJ*, 583, 124
- Strateva, I., et al. 2001, *AJ*, 122, 1861
- Strauss, M. A., et al. 2002, *AJ*, 124, 1810
- Thim, F., Hoessel, J. G., Saha, A., Claver, J., Dolphin, A., & Tammann, G. A. 2004, *AJ*, 127, 2322
- Thornton, C. E., Barth, A. J., Ho, L. C., Rutledge, R. E., & Greene, J. E. 2008, *ApJ*, submitted
- Tran, H. D. 2003, *ApJ*, 583, 632
- Tremaine, S., et al. 2002, *ApJ*, 574, 740
- Turnshek, D. A., Bohlin, R. C., Williamson, R. L., II, Lupie, O. L., Koornneef, J., & Morgan, D. H. 1990, *AJ*, 99, 1243
- Ulvestad, J. S., & Ho, L. C. 2001, *ApJ*, 558, 561
- Valluri, M., Ferrarese, L., Merritt, D., & Joseph, C. L. 2005, *ApJ*, 628, 137
- Voges, W., et al. 1999, *A&A*, 349, 389
- Wang, T., & Lu, Y. 2001, *A&A*, 377, 52
- Whittle, M. 1985, *MNRAS*, 213, 1
- Whittle, M., Pedlar, A., Meurs, E. J. A., Unger, S. W., Axon, D. J., & Ward, M. J. 1988, *ApJ*, 326, 125
- Wytthe, J. S. B. 2006, *MNRAS*, 365, 1082
- Zakamska, N. L., et al. 2003, *AJ*, 126, 2125
- Zhou, H., Wang, T., Zhang, X., Dong, X., & Li, C. 2004, *ApJ*, 604, L33

TABLE 1
 SAMPLE PROPERTIES

| Galaxy | Plate/MJD/Fiber | z | M_g (mag) | $\log M_*$ (M_\odot) | $\log L([\text{O III}])$ (L_\odot) | C | References |
|--------------------------|-----------------|--------|----------------|-----------------------------|---|------|------------|
| SDSS J010053.57+152728.1 | 421.51821.461 | 0.0404 | -19.5 | 9.75 | 5.83 | 2.59 | a,b |
| SDSS J011059.31+002601.1 | 397.51794.474 | 0.0188 | -18.7 | 9.81 | 6.23 | 2.46 | a |
| SDSS J011905.14+003745.0 | 398.51789.585 | 0.0327 | -17.6 | 9.16 | 6.64 | 3.26 | a,b |
| SDSS J021405.91-001637.0 | 405.51816.168 | 0.0373 | -18.9 | 9.72 | 7.37 | 2.74 | a,b |
| SDSS J034330.26-073507.4 | 462.51909.044 | 0.0357 | -18.7 | 9.61 | 5.81 | 2.84 | a,b |
| SDSS J091414.34+023801.8 | 567.52252.259 | 0.0735 | -19.7 | 9.97 | 7.56 | 2.78 | a |
| SDSS J091608.50+502126.9 | 766.52247.197 | 0.0495 | -18.8 | 9.90 | 6.39 | 2.64 | a |
| SDSS J094716.13+534944.9 | 769.52282.240 | 0.0383 | -18.5 | 9.56 | 6.78 | 2.85 | a |
| SDSS J100654.83+445642.8 | 943.52376.222 | 0.0419 | -19.0 | 10.1 | 6.99 | 3.20 | a |
| SDSS J102332.00+645240.2 | 489.51930.308 | 0.0404 | -19.2 | 9.78 | 6.17 | 2.76 | a,b |
| SDSS J103126.56+624648.6 | 772.52375.548 | 0.0529 | -19.4 | 10.50 | 7.55 | 2.49 | a |
| SDSS J103234.85+650227.9 | 489.51930.193 | 0.0056 | -18.6 | ... | 4.85 | 2.29 | b,c |
| SDSS J105308.99+041036.2 | 579.52338.107 | 0.0431 | -18.5 | 9.54 | 6.61 | 2.61 | a |
| SDSS J110912.40+612346.7 | 775.52295.309 | 0.0067 | -16.8 | 8.07 | 4.94 | 1.95 | a |
| SDSS J111255.26+552928.8 | 909.52379.249 | 0.0498 | -19.1 | 9.86 | 6.53 | 2.53 | a |
| SDSS J114315.36+631108.2 | 776.52319.604 | 0.0622 | -19.4 | 9.68 | 7.16 | 2.37 | a |
| SDSS J120815.94+512325.7 | 882.52370.012 | 0.0331 | -18.3 | 9.60 | 6.54 | 2.45 | a |
| SDSS J130525.75+642121.5 | 602.52072.172 | 0.0527 | -19.5 | 10.41 | 7.37 | 2.41 | a,b |
| SDSS J142151.63+033121.2 | 584.52049.218 | 0.0552 | -18.9 | 9.59 | 6.66 | 2.76 | a |
| SDSS J143231.15+004614.4 | 535.51999.049 | 0.0712 | -19.5 | 9.97 | 7.65 | 2.50 | a,b |
| SDSS J143534.96+591658.3 | 790.52441.409 | 0.0682 | -19.4 | 10.41 | 7.51 | 2.48 | a |
| SDSS J144012.70+024743.5 | 536.52024.575 | 0.0298 | -19.0 | ... | 7.43 | 2.72 | b,d,e |
| SDSS J151135.60+023807.0 | 540.51996.524 | 0.0389 | -19.2 | 9.71 | 6.89 | 2.83 | a,b |
| SDSS J155404.40+545708.2 | 619.52056.448 | 0.0457 | -18.8 | 9.98 | 6.46 | 2.45 | a,b |
| SDSS J160428.50-010435.7 | 344.51693.053 | 0.0296 | -19.4 | 9.78 | 6.45 | 2.74 | a |
| SDSS J160510.73+472901.5 | 813.52354.558 | 0.0435 | -19.0 | 9.85 | 6.08 | 2.85 | a |
| SDSS J161038.31+522334.2 | 623.52051.381 | 0.0617 | -19.4 | 10.04 | 6.51 | 1.95 | a,b |
| SDSS J162917.44+425439.8 | 815.52374.032 | 0.0353 | -18.1 | 9.61 | 7.44 | 2.24 | a |
| SDSS J172344.17+583032.2 | 366.52017.274 | 0.0780 | -19.7 | 10.16 | 7.61 | 2.55 | a,b |

NOTE. — “Plate/MJD/Fiber” gives the reference to the SDSS spectroscopic observation of each object, for cross-identification in the SDSS archives. References for previous AGN identifications are: (a) Kauffmann et al. (2003b) with updated data from <http://www.mpa-garching.mpg.de/SDSS>; (b) Hao et al. (2005a); (c) Moran et al. (1996); (d) Bohuski et al. (1978); (e) Anderson et al. (2003). Stellar masses, [O III] luminosities, velocity dispersions, and concentration indices C are from the Kauffmann et al. online catalog, except for 1032+6502 and 1440+0247; for these two objects the concentration indices are from the SDSS database and $L([\text{O III}])$ is determined from the extinction-corrected [O III] flux and the galaxy distance. Absolute g -band magnitudes are corrected for Galactic extinction using the Schlegel et al. (1998) extinction maps and k -corrected using M. Blanton’s *kcorrect* code.

TABLE 2
VELOCITY DISPERSIONS AND LINEWIDTHS

| Galaxy | Exp. Time (s) | S/N | σ_* (km s ⁻¹) | σ ([O III]) (km s ⁻¹) | FWHM([O III]) (km s ⁻¹) | FWHM([S II]) (km s ⁻¹) |
|---------------------|------------------|------|-------------------------------------|---|--|---------------------------------------|
| J010053.57+152728.1 | 900 | 10.9 | 52 ± 4 | 36 ± 2 | 86 ± 4 | 77 ± 9 |
| J011059.31+002601.1 | 3600 | 40.4 | 63 ± 5 | 88 ± 3 | 143 ± 11 | 157 ± 2 |
| J011905.14+003745.0 | 900 | 8.4 | 39 ± 8 | 66 ± 2 | 77 ± 3 | 90 ± 3 |
| J021405.91-001637.0 | 3600 | 35.6 | 59 ± 5 | 181 ± 1 | 159 ± 1 | 142 ± 2 |
| J034330.26-073507.4 | 3600 | 45.8 | 94 ± 3 | 75 ± 1 | 223 ± 3 ^a | ... ^a |
| J091414.34+023801.8 | 1800 | 6.1 | 65 ± 12 | 68 ± 1 | 152 ± 4 ^a | 164 ± 13 |
| J091608.50+502126.9 | 1800 | 11.6 | 48 ± 3 | 75 ± 3 | 96 ± 8 | 75 ± 2 |
| J094716.13+534944.9 | 1800 | 14.5 | 55 ± 3 | 77 ± 1 | 147 ± 1 | 129 ± 1 |
| J100654.83+445642.8 | 1800 | 12.0 | 65 ± 5 | 147 ± 13 | 428 ± 7 ^a | ... ^a |
| J102332.00+645240.2 | 1800 | 16.8 | 56 ± 5 | 57 ± 1 | 145 ± 3 | 161 ± 5 |
| J103126.56+624648.6 | 1800 | 7.1 | 72 ± 9 | 85 ± 4 | 138 ± 13 | 236 ± 5 |
| J103234.85+650227.9 | 1800 | 25.2 | 43 ± 4 | 69 ± 1 | 71 ± 4 | 53 ± 2 |
| J105308.99+041036.2 | 1800 | 2.6 | ... | 84 ± 8 | 134 ± 24 | 125 ± 18 |
| J110912.40+612346.7 | 1700 | 3.4 | ... | 28 ± 1 | 66 ± 1 | 63 ± 2 |
| J111255.26+552928.8 | 1800 | 12.7 | 67 ± 4 | 69 ± 1 | 109 ± 4 | 128 ± 5 |
| J114315.36+631108.2 | 1800 | 14.7 | 70 ± 9 | 123 ± 2 | 168 ± 3 | 152 ± 8 |
| J120815.94+512325.7 | 1800 | 4.6 | 47 ± 8 | 74 ± 2 | 174 ± 8 | 153 ± 7 |
| J130525.75+642121.5 | 1800 | 9.9 | 77 ± 4 | 70 ± 3 | 166 ± 8 | 218 ± 4 |
| J142151.63+033121.2 | 1800 | 18.4 | 50 ± 4 | 62 ± 1 | 71 ± 2 | 66 ± 2 |
| J143231.15+004614.4 | 1800 | 7.9 | 65 ± 8 | 75 ± 6 | 138 ± 14 | 118 ± 9 |
| J143534.96+591658.3 | 1800 | 11.1 | 91 ± 6 | 96 ± 4 | 162 ± 10 | 172 ± 7 |
| J144012.70+024743.5 | 3600 | 32.0 | 45 ± 4 | 122 ± 1 | 108 ± 1 | 105 ± 1 |
| J151135.60+023807.0 | 1800 | 29.3 | 65 ± 5 | 95 ± 2 | 131 ± 4 | 135 ± 6 |
| J155404.40+545708.2 | 1800 | 25.0 | 73 ± 3 | 62 ± 1 | 72 ± 1 | 63 ± 3 |
| J160428.50-010435.7 | 1800 | 20.2 | 56 ± 4 | 97 ± 2 | 94 ± 4 | 103 ± 2 |
| J160510.73+472901.5 | 1800 | 19.7 | 67 ± 3 | 149 ± 5 | 217 ± 14 | 197 ± 6 |
| J161038.31+522334.2 | 1800 | 8.1 | 59 ± 7 | 88 ± 4 | 152 ± 12 | 158 ± 9 |
| J162917.44+425439.8 | 1800 | 17.3 | 61 ± 4 | 238 ± 1 | 90 ± 2 ^a | 141 ± 2 ^{ab} |
| J172344.17+583032.2 | 1800 | 15.0 | 66 ± 6 | 105 ± 3 | 193 ± 6 | 154 ± 3 |

NOTE. — S/N is the mean signal-to-noise ratio per pixel in the extracted ESI spectrum over the wavelength range 5200–5600 Å.

^a[O III] profile is double-peaked.

TABLE 3
EMISSION LINES IN THE COMPOSITE SEYFERT 2 SPECTRUM

| Line | $f/f(H\beta)$ |
|---------------------------|-----------------|
| [Ne III] λ 3868 | 0.55 ± 0.04 |
| [Ne III] λ 3967 | 0.15 ± 0.01 |
| H ϵ | 0.15 ± 0.01 |
| [S II] λ 4068 | 0.08 ± 0.01 |
| H δ | 0.22 ± 0.02 |
| H γ | 0.41 ± 0.02 |
| [O III] λ 4363 | 0.07 ± 0.01 |
| He I λ 4471 | 0.03 ± 0.01 |
| He II λ 4686 | 0.20 ± 0.02 |
| [Ar IV] λ 4711 | 0.04 ± 0.01 |
| [Ar IV] λ 4740 | 0.04 ± 0.01 |
| H β | 1.00 ± 0.03 |
| [O III] λ 4959 | 2.07 ± 0.06 |
| [O III] λ 5007 | 6.47 ± 0.16 |
| [N I] λ 5199,5201 | 0.12 ± 0.01 |
| He I λ 5876 | 0.12 ± 0.01 |
| [Fe VII] λ 6086 | 0.04 ± 0.01 |
| [O I] λ 6300 | 0.52 ± 0.02 |
| [S III] λ 6312 | 0.05 ± 0.01 |
| [O I] λ 6363 | 0.22 ± 0.02 |
| [N II] λ 6548 | 0.95 ± 0.11 |
| H α | 4.63 ± 0.15 |
| [N II] λ 6583 | 2.64 ± 0.12 |
| He I λ 6678 | 0.02 ± 0.01 |
| [S II] λ 6716 | 1.18 ± 0.03 |
| [S II] λ 6731 | 0.99 ± 0.03 |
| [Ar III] λ 7135 | 0.19 ± 0.01 |
| [O II] λ 7310 | 0.09 ± 0.01 |
| [O II] λ 7331 | 0.10 ± 0.01 |
| [S III] λ 9069 | 0.74 ± 0.05 |
| [S III] λ 9532 | 1.93 ± 0.12 |

NOTE. — Line strengths measured from the composite Seyfert 2 spectrum are given relative to H β . The spectrum is corrected for Galactic extinction but not for internal extinction within the host galaxies.

TABLE 4
POLARIZATION DATA

| Galaxy | S/N | p_b (%) | θ_b (degrees) | p_r (%) | θ_r (degrees) | $E(B-V)$ (mag) | $p_{\max}(\text{Galactic})$ (%) |
|---------------------|------|-----------------|-------------------------|-----------------|-------------------------|-------------------|------------------------------------|
| J011905.14+003745.0 | 80 | 0.55 ± 0.06 | 111 ± 3 | 0.29 ± 0.05 | 119 ± 6 | 0.032 | 0.29 |
| J021405.91-001637.0 | 160 | 0.50 ± 0.03 | 160 ± 2 | 0.52 ± 0.03 | 159 ± 2 | 0.038 | 0.34 |
| J094716.13+534944.9 | 105 | 0.22 ± 0.04 | 33 ± 5 | 0.20 ± 0.04 | 25 ± 5 | 0.014 | 0.13 |
| J110912.40+612346.7 | 42 | 0.76 ± 0.10 | 69 ± 4 | 0.72 ± 0.10 | 72 ± 4 | 0.011 | 0.10 |
| HD 57702 (null) | 1060 | 0.07 ± 0.01 | 161 ± 1 | 0.08 ± 0.01 | 150 ± 2 | | |

NOTE. — S/N is the signal-to-noise per pixel over the continuum wavelength range 6380–6480 Å in the total flux spectrum. Polarization on the blue and red sides (p_b , p_r) and polarization angles (θ_b , θ_r) are measured over the wavelength regions 4000–5500 and 6000–7500 Å. Galactic reddening estimates are from Schlegel et al. (1998), and the maximum estimated Galactic foreground polarization is $p_{\max}(\%) = 9.0 \times E(B-V)$ (Serkowski et al. 1975).

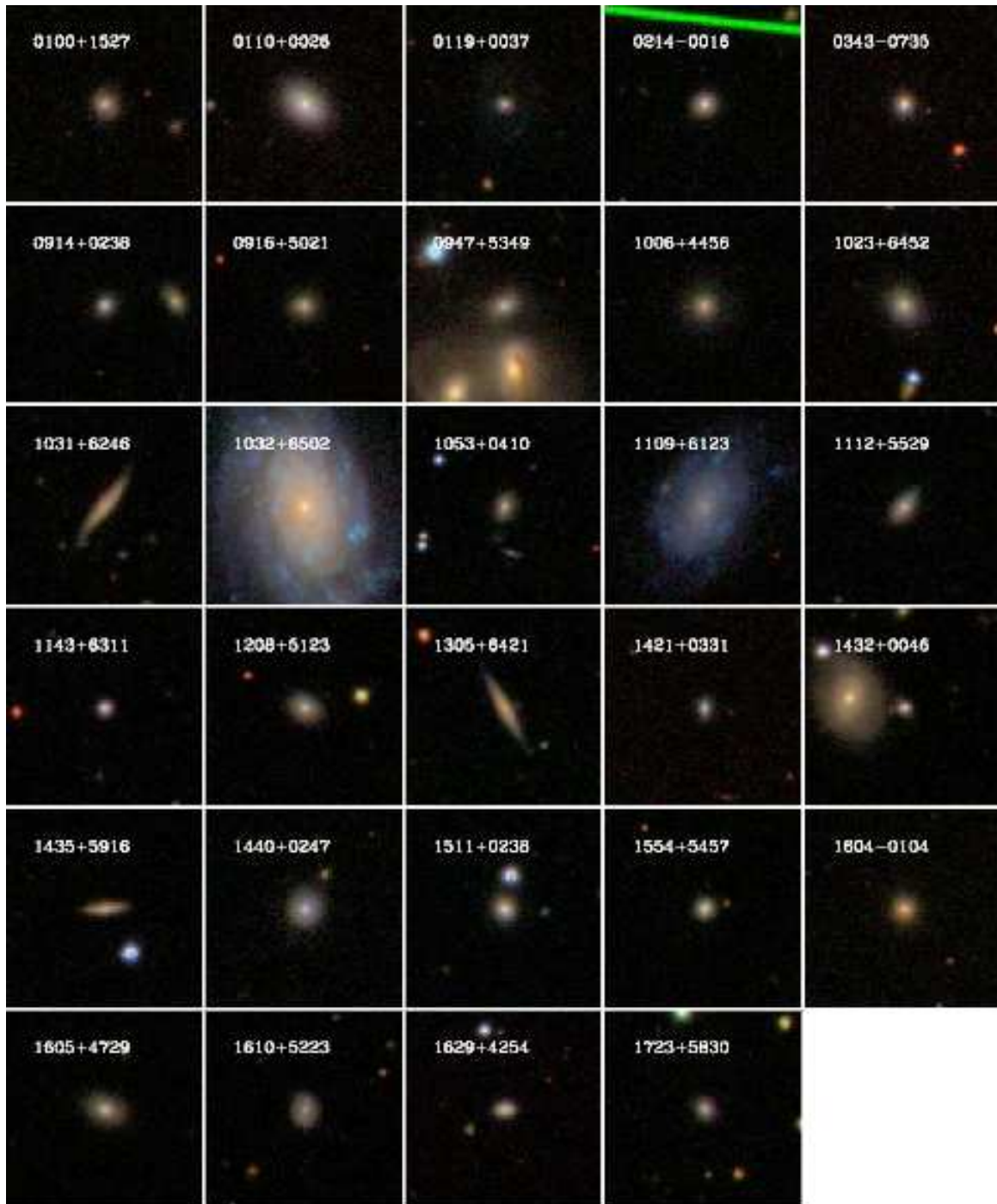


FIG. 1.— SDSS color composite images of the Seyfert galaxy sample. The image size is $1' \times 1'$. North is up and east is to the left.

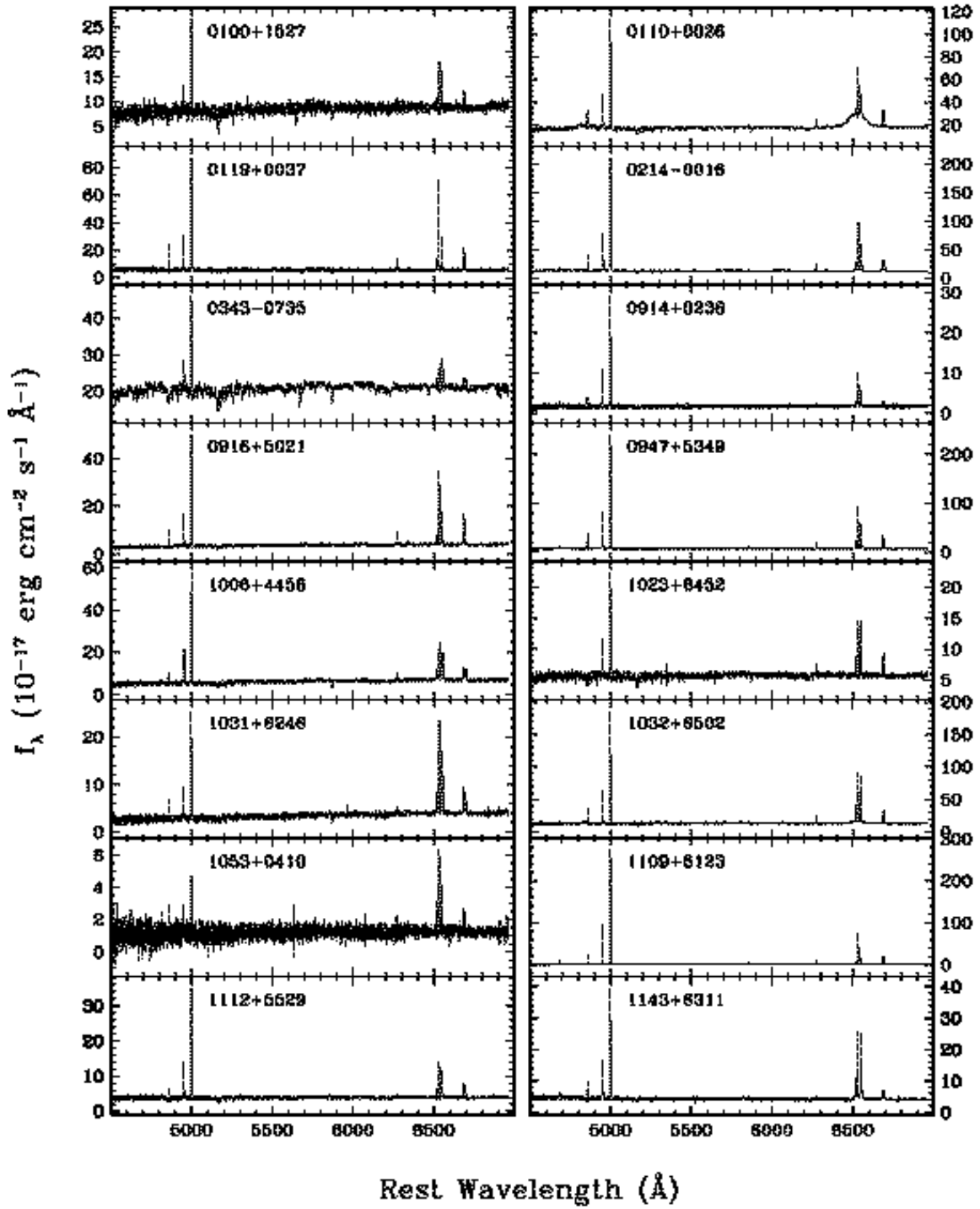


FIG. 2.— Central portions of the Keck ESI spectra of the SDSS Seyfert sample. The spectra are binned to $0.5 \text{ \AA pixel}^{-1}$ for clarity.

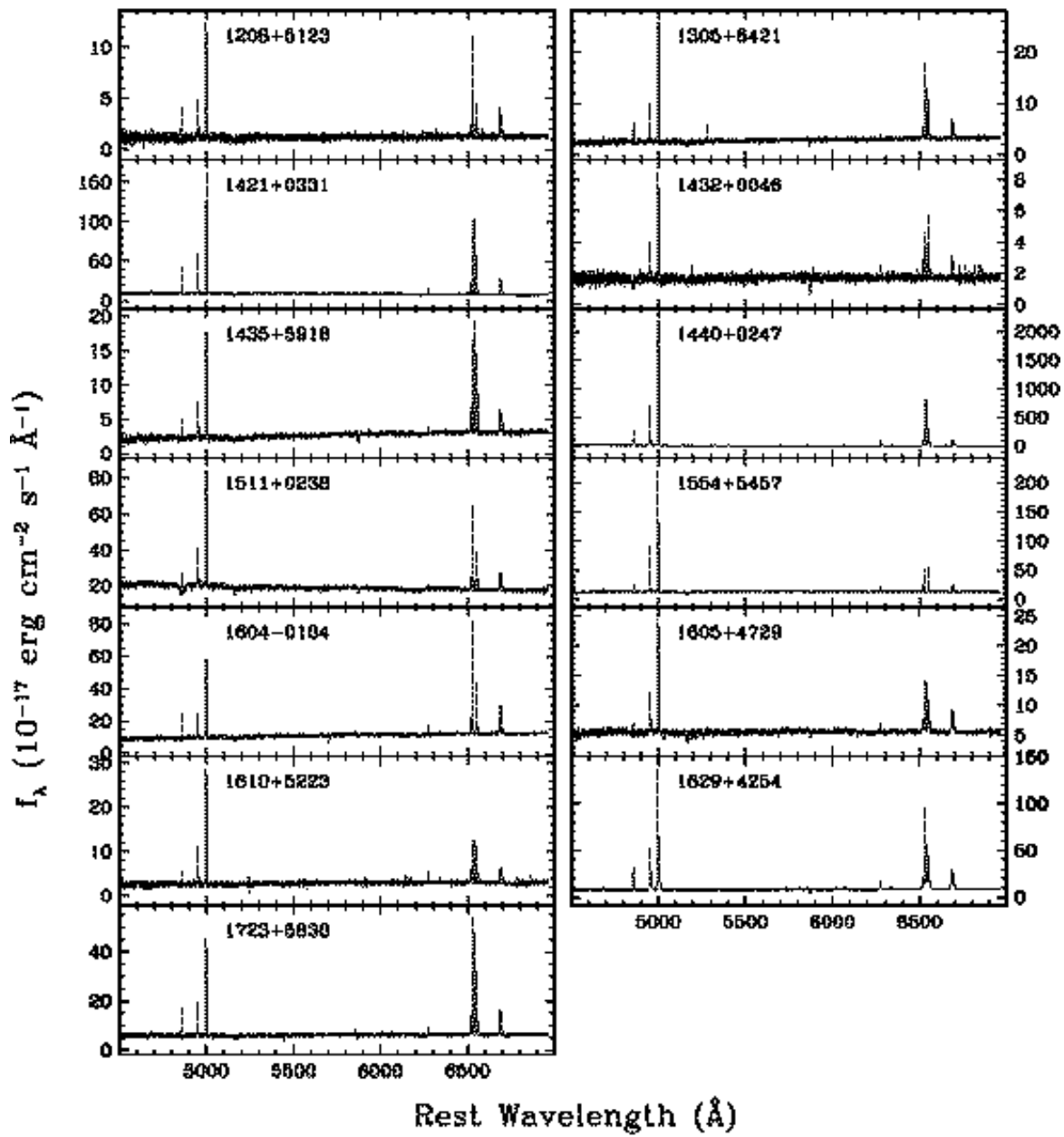


FIG. 2.— (Continued) Keck ESI spectra of the SDSS Seyfert sample.

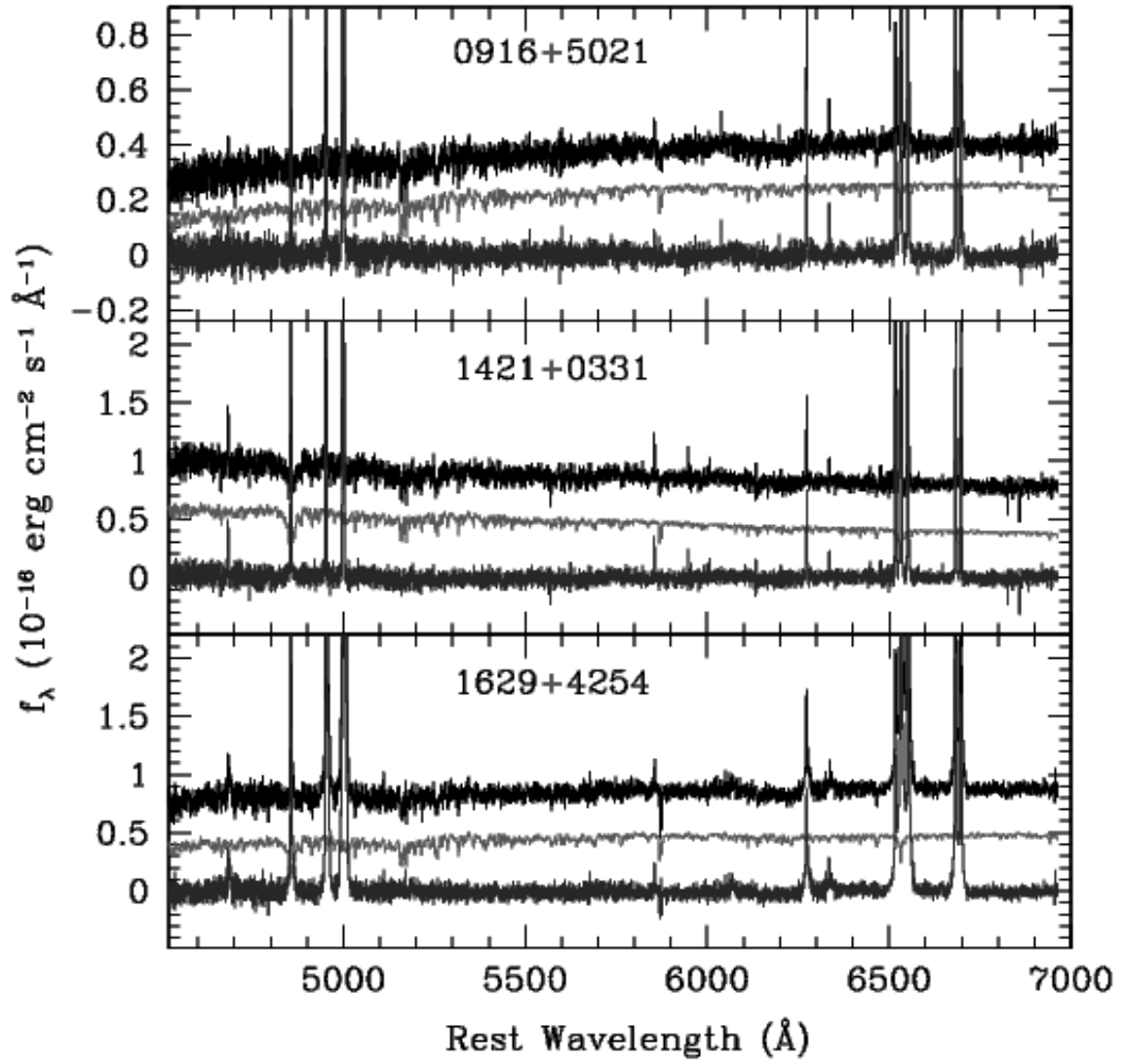


FIG. 3.— Examples of starlight subtraction. In each panel, the galaxy spectrum is in black, the best-fitting model is in red, and the starlight-subtracted spectrum is in blue. The model spectra are shifted downward by a constant offset for clarity.

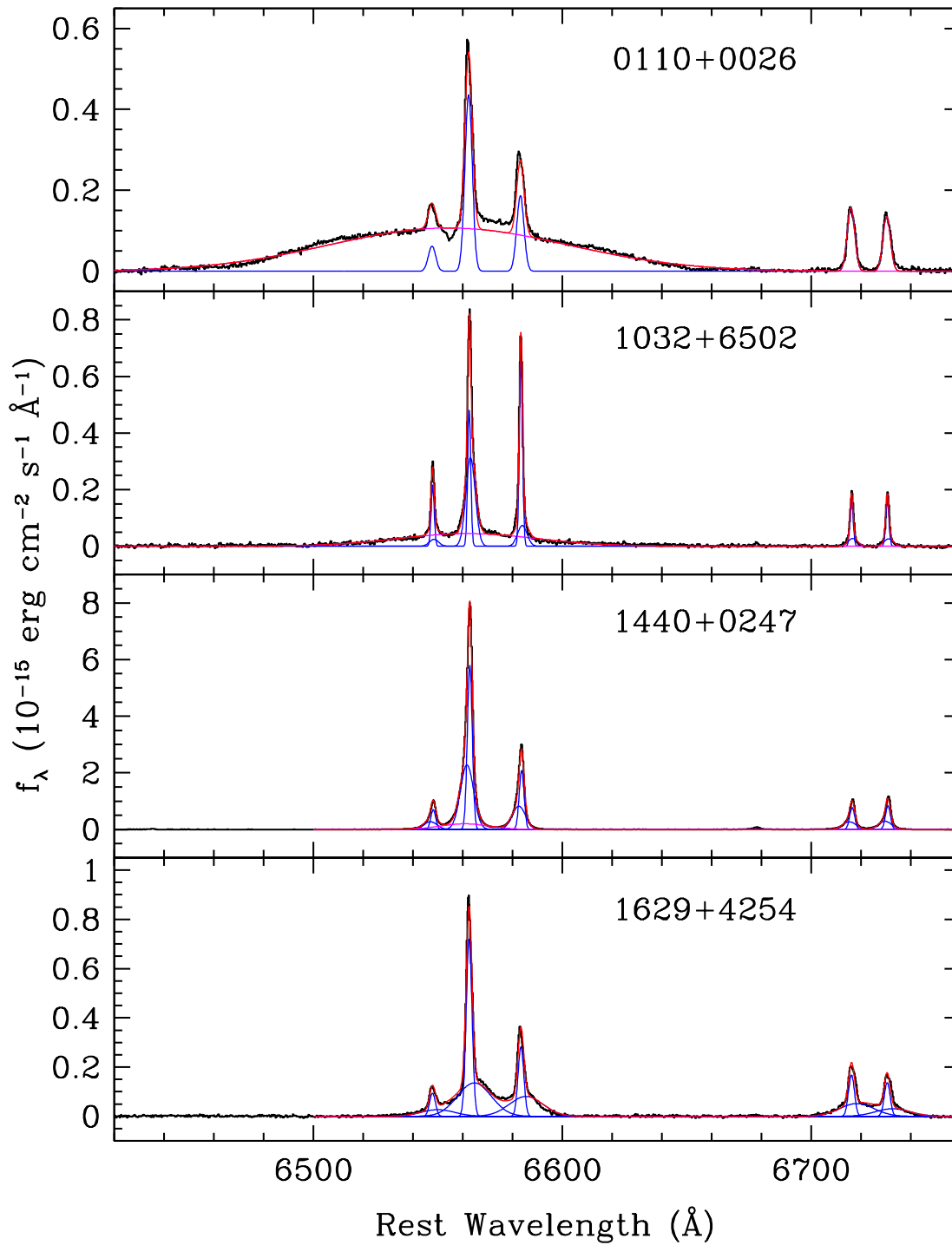


FIG. 4.— Multi-Gaussian fits to the $H\alpha$, $[\text{N II}]$, and $[\text{S II}]$ lines for four objects, after starlight subtraction. In each plot, the narrow-line components are plotted in blue, the broad components in magenta, and the sum of all model components in red. For the galaxy 1629+4254, all of the narrow lines contain the redshifted wing component, and the $H\alpha$ profile does not require an additional broad component.

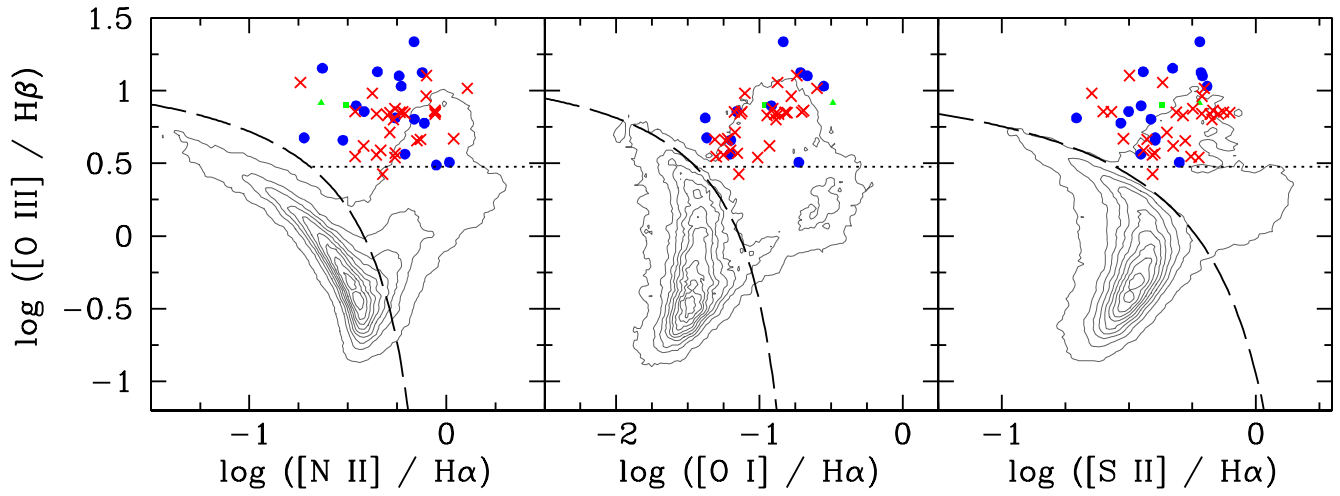


FIG. 5.— Line-ratio diagrams for $[\text{O III}] \lambda 5007 / \text{H}\beta$ versus $[\text{N II}] \lambda 6583 / \text{H}\alpha$, $[\text{S II}] \lambda 6716, 6731 / \text{H}\alpha$, and $[\text{O I}] \lambda 6300 / \text{H}\alpha$. Grey contours represent emission-line galaxies from Kauffmann et al. (2003b) with $S/N > 6$ in $\text{H}\alpha$, $[\text{O III}]$, and $[\text{N II}]$, and $S/N > 3$ in $[\text{O I}]$ flux. Blue circles are the Seyfert 1 galaxies from Greene & Ho (2004), and red crosses are measurements from the Keck data for the Seyfert sample described here. NGC 4395 and POX 52 are shown as a green triangle and square. Dashed curves are the “maximum starburst” lines from Kewley et al. (2006), and the horizontal dotted line shows the selection cut at $[\text{O III}]/\text{H}\beta = 3$.

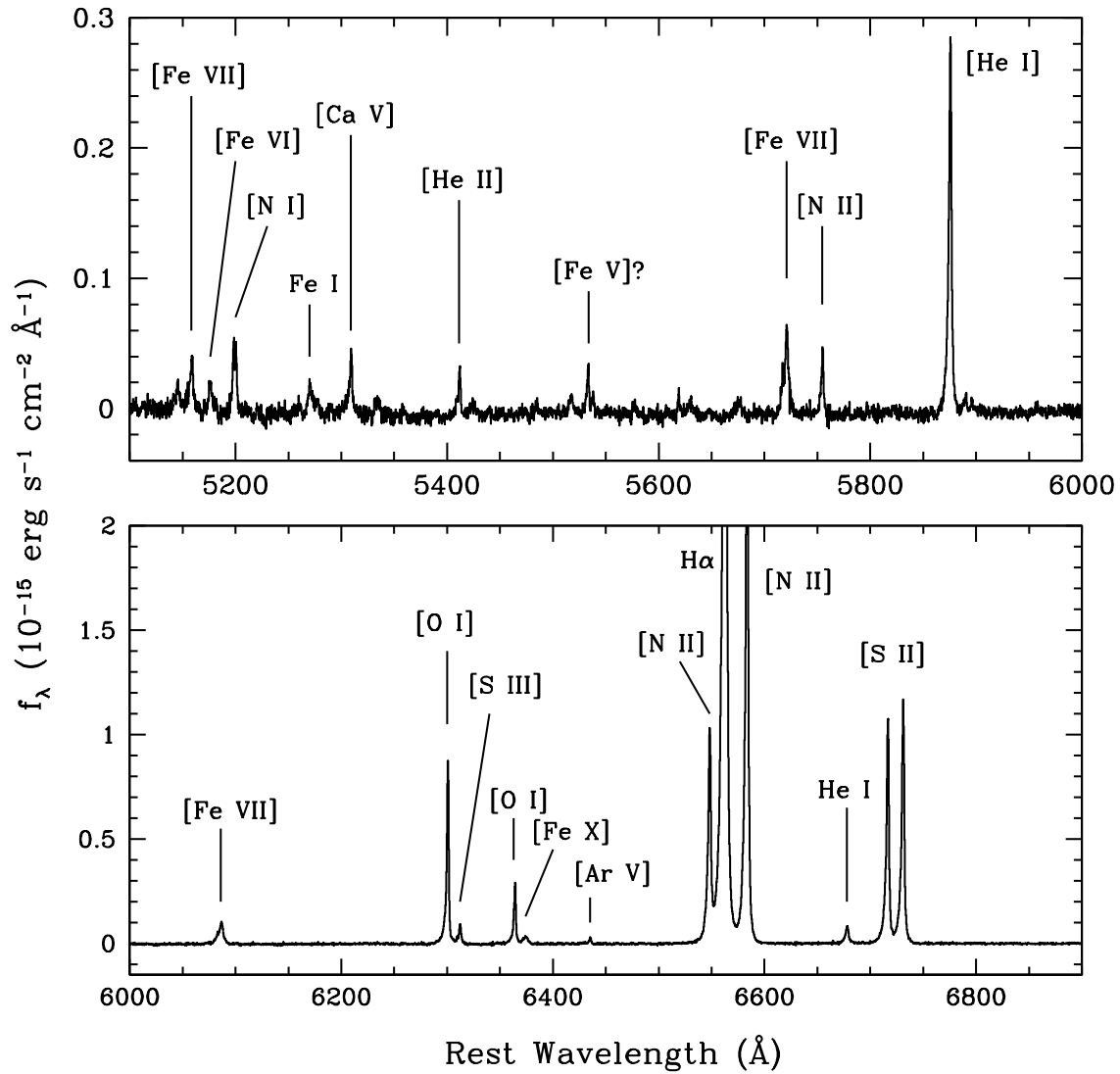


FIG. 6.— Two sections of the starlight-subtracted ESI spectrum of SDSS J144012.70+024743.5, showing coronal-line emission including lines of [Fe VII] and [Fe X]. [Fe XI] emission is also present at 7892 Å.

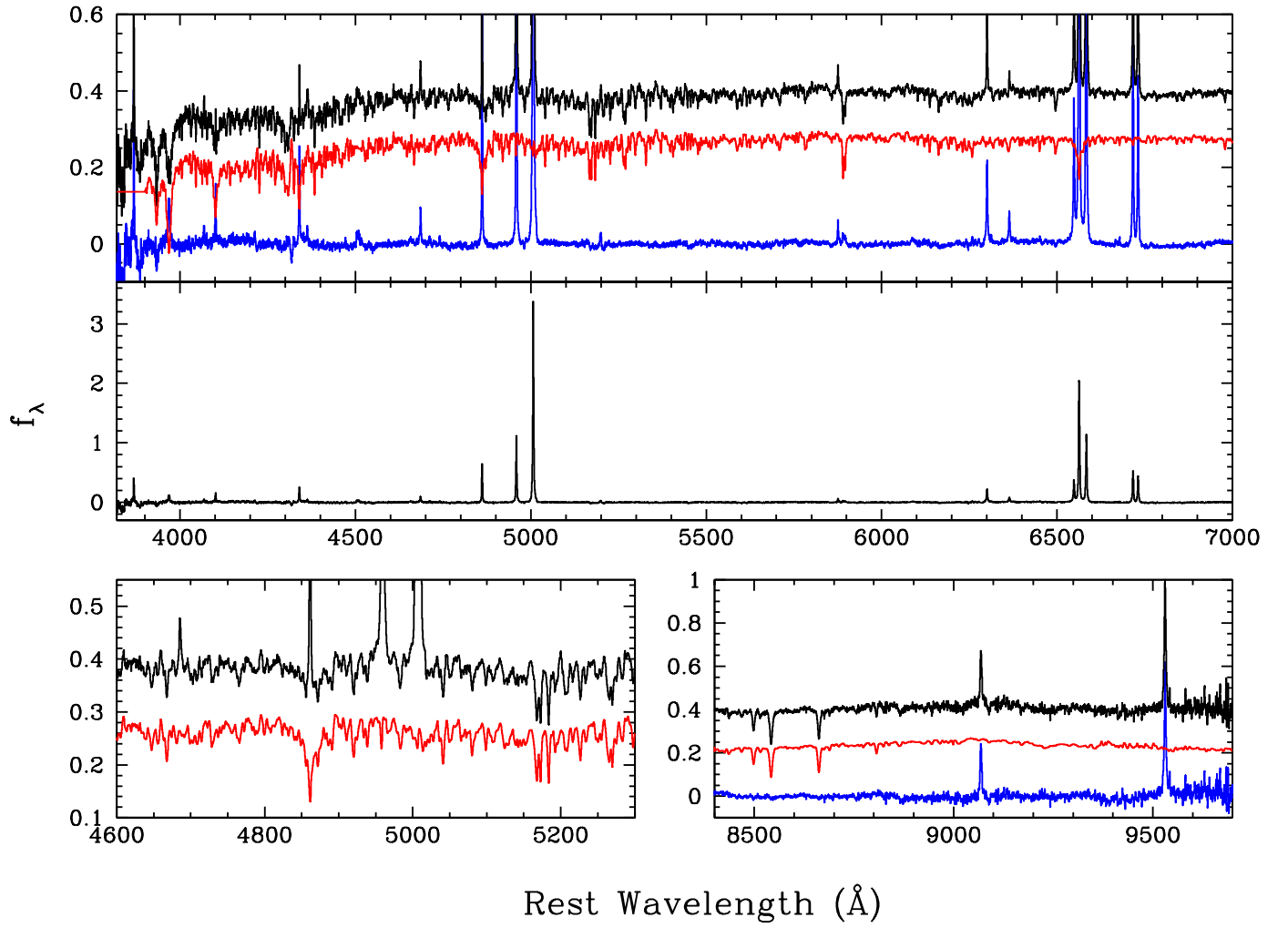


FIG. 7.— Composite Seyfert 2 spectrum. *Upper panel:* Composite spectrum (in black), model fit from the starlight subtraction routine (red), and starlight-subtracted spectrum (blue). *Middle panel:* Expanded view of the emission-line spectrum after starlight subtraction. *Bottom panels:* Expanded views of the region including $H\beta$ and the Mgb lines (left) and the Ca II triplet and [S III] $\lambda\lambda 9069, 9532 \text{ \AA}$ emission lines. The model spectra (red) are shifted downward by a constant offset for clarity.

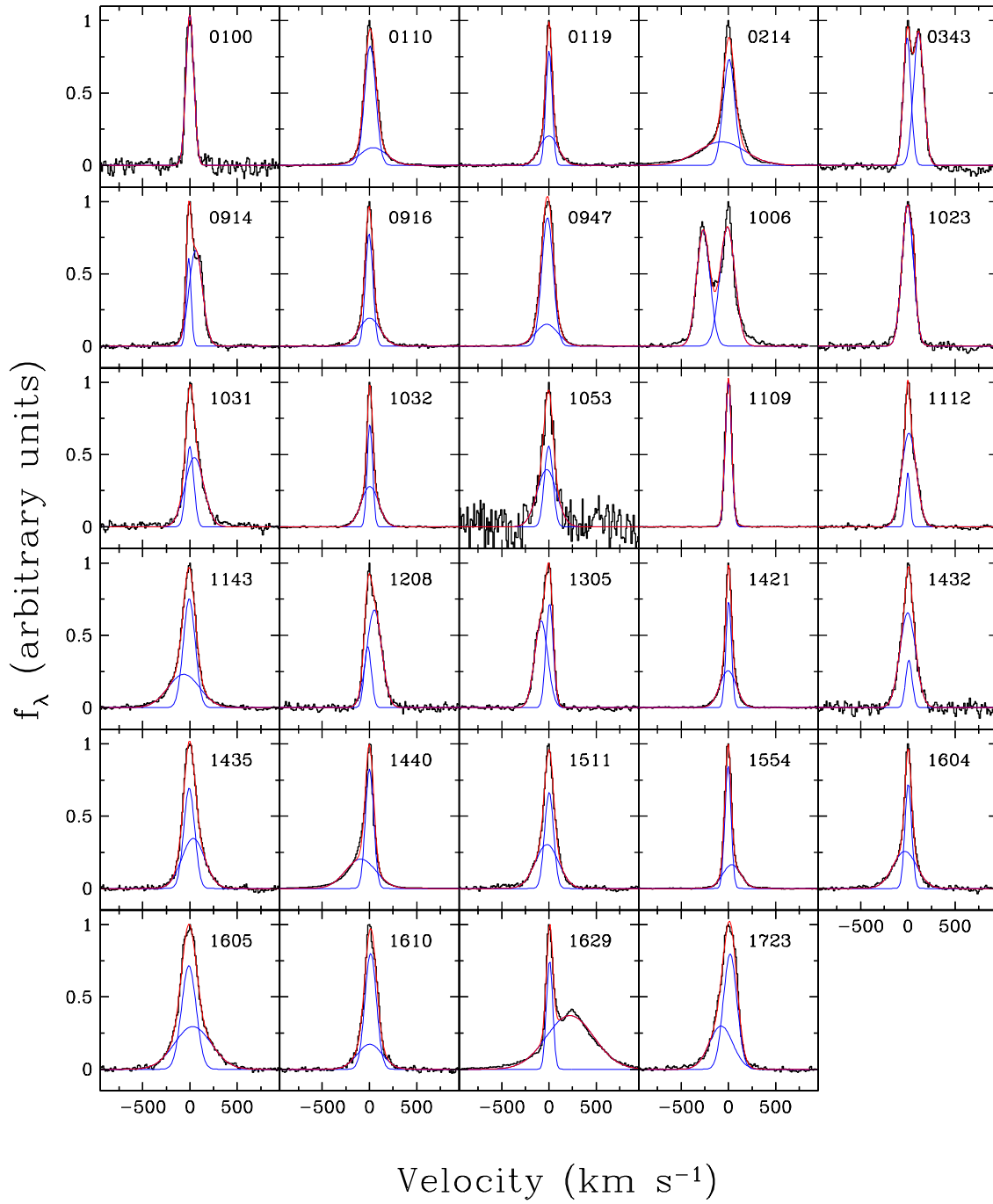


FIG. 8.— [O III] $\lambda 5007$ profiles with single or double-Gaussian model fits. Individual Gaussian components are shown in blue and the summed model is in red.

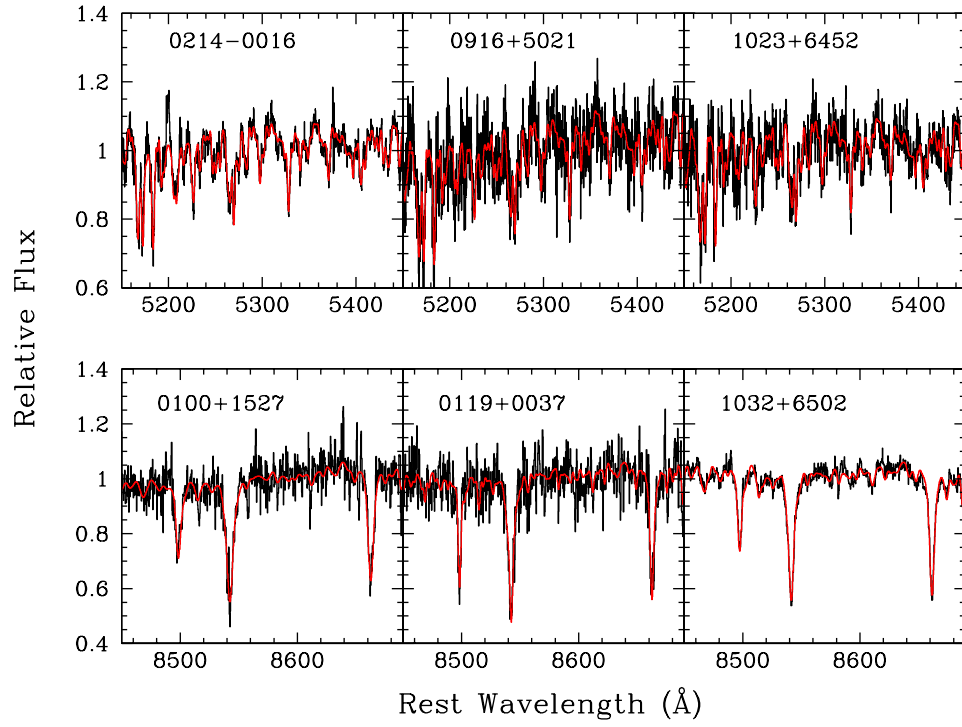


FIG. 9.— Examples of fits from velocity dispersion measurements, illustrating the range of data quality for the Keck observations. Upper panels show fits to the *Mgb* spectral region and lower panels show the Ca II triplet region. The spectrum in red is the best-fitting broadened K-giant template star.

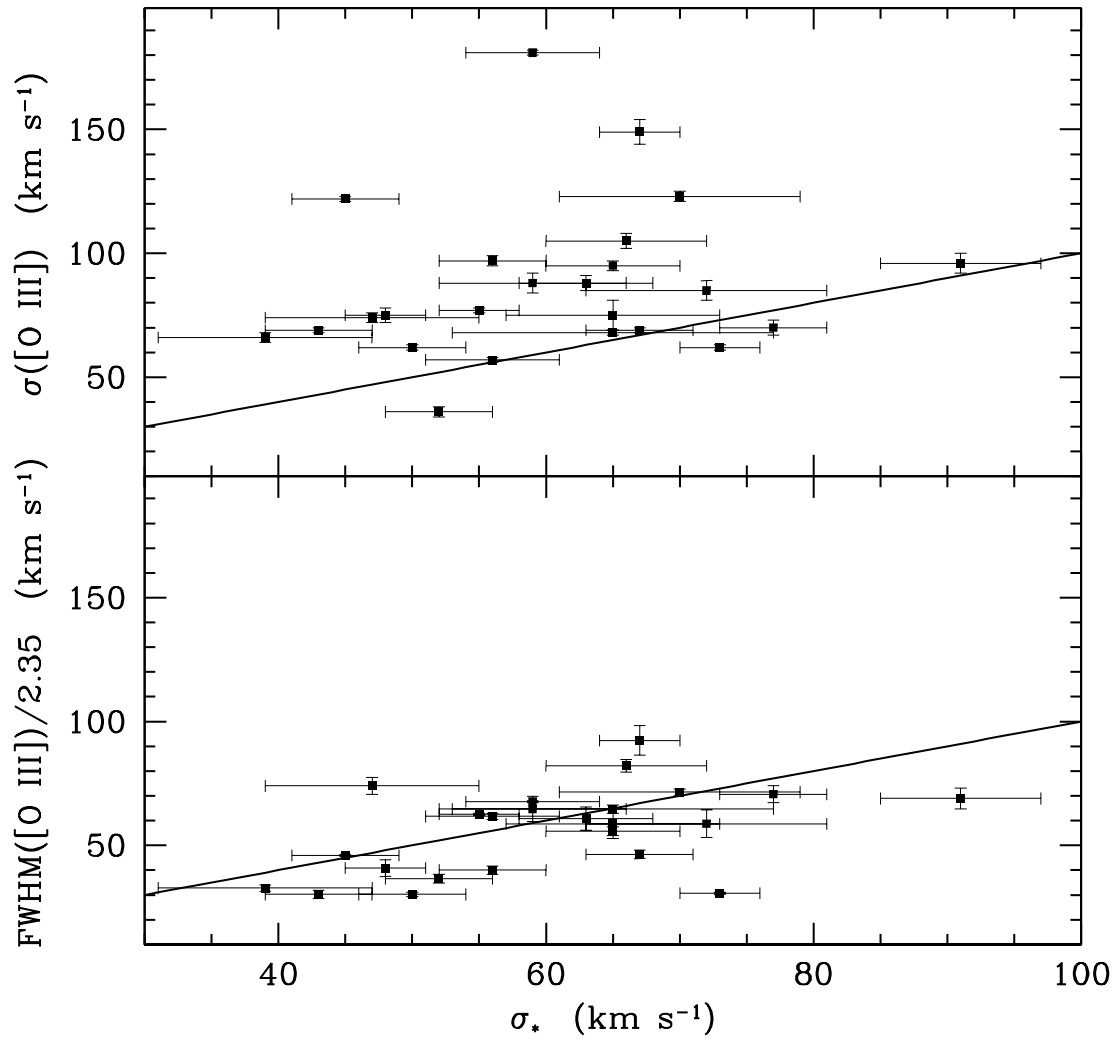


FIG. 10.— Comparison of stellar and emission-line velocity dispersions. The upper panel shows the line dispersion $\sigma_{[\text{O III}]}$, and the lower panel shows $\text{FWHM}_{[\text{O III}]} / 2.35$. The solid line in each panel represents a 1:1 correspondence between stellar and gas linewidths. Objects with double-peaked profiles are not included.

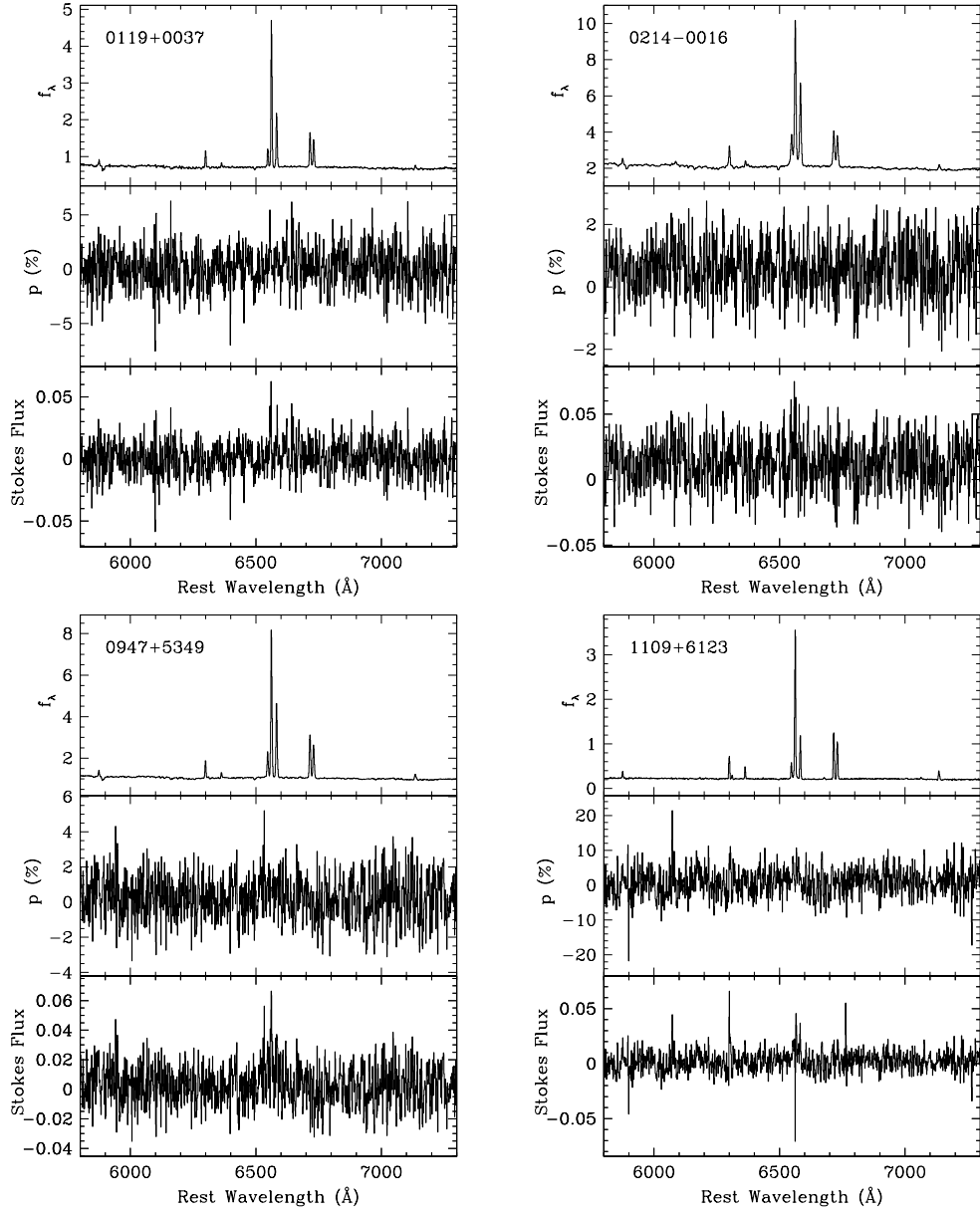


FIG. 11.— Keck LRIS polarimetry data for four objects in the spectral region surrounding the H α emission line. In each plot, the top panel is the total flux spectrum in units of $10^{-16} \text{ erg s}^{-1} \text{ cm}^{-2} \text{ \AA}^{-1}$, the middle panel is the percent polarization given in the form of the rotated Stokes parameter, and the bottom panel is the Stokes flux $p \times f_\lambda$.

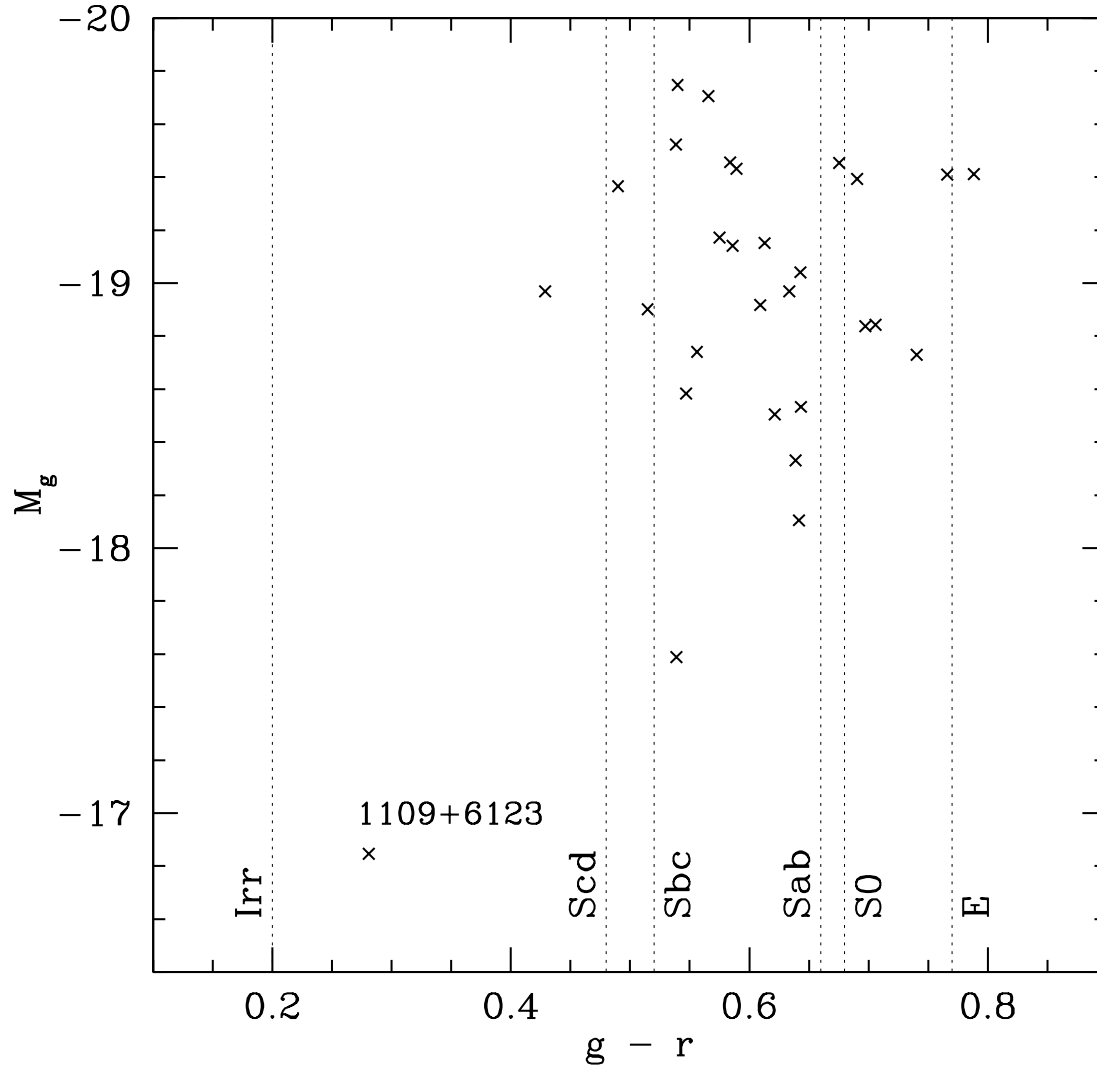


FIG. 12.— Color-magnitude diagram for the galaxies in this sample, based on SDSS photometry. Standard colors for different Hubble types are from Fukugita et al. (1995).

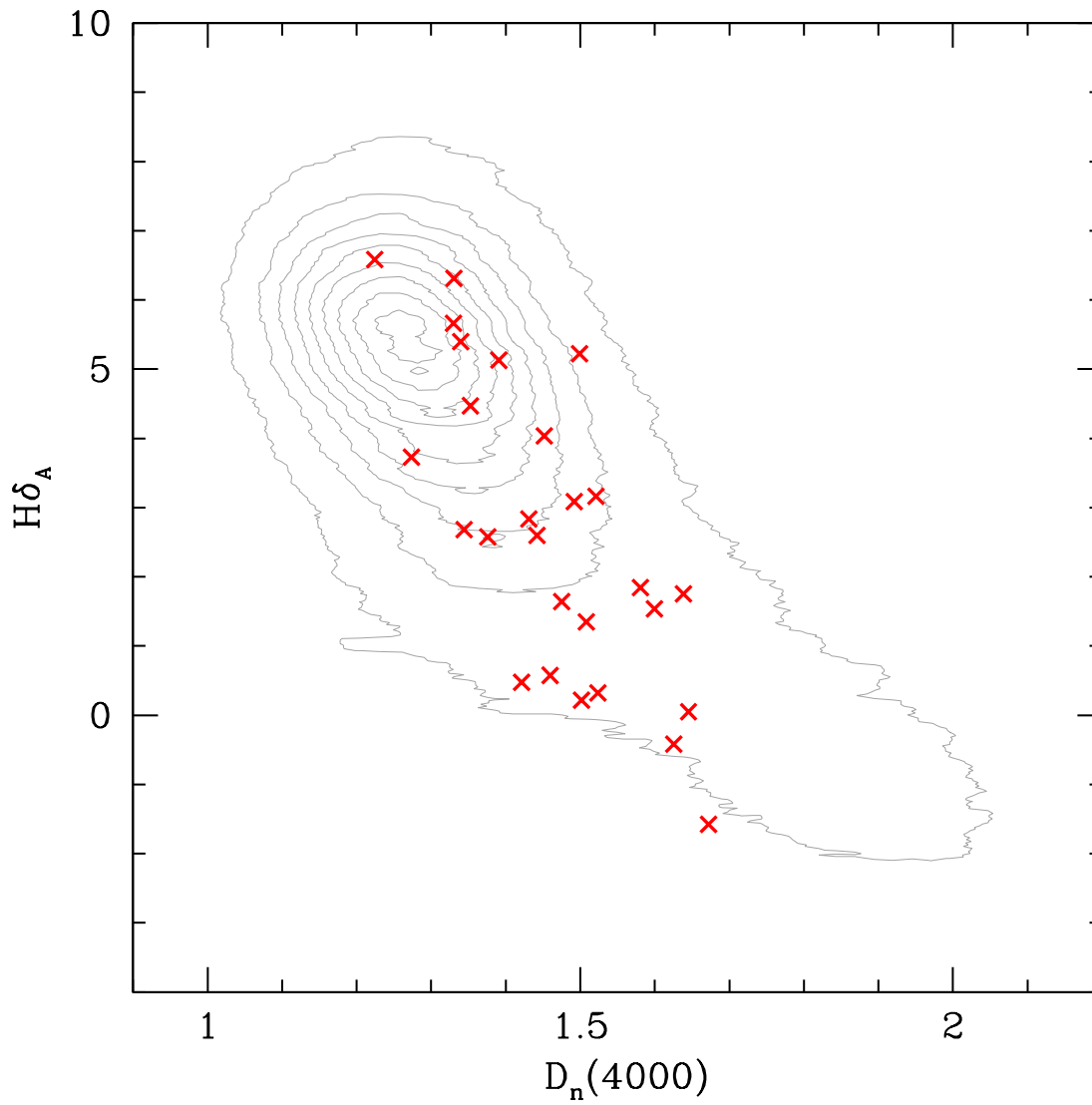


FIG. 13.— The $D_n(4000)$ and $H\delta_A$ indices for this sample (red crosses). Grey contours and small dots represent the distribution of galaxies from the Kauffmann et al. (2003b) sample within the mass range $9.0 < \log(M/M_\odot) < 10.0$.

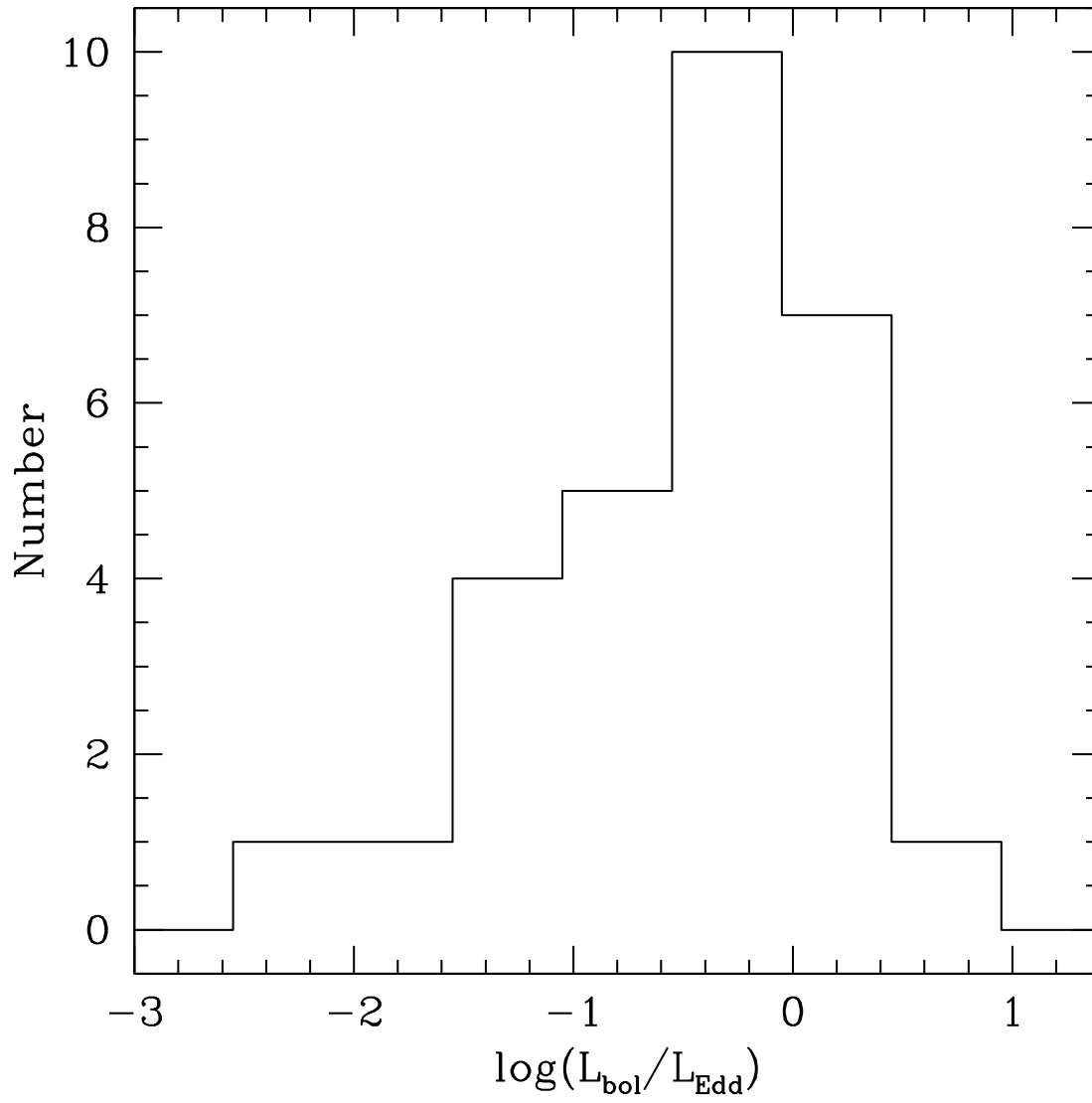


FIG. 14.— Eddington ratio $L_{\text{bol}}/L_{\text{Edd}}$ for our sample, based on the assumptions of an [O III] bolometric correction of $L_{\text{bol}}/L([\text{O III}])=3500$ (Heckman et al. 2004) and an offset of 0.23 dex from the Tremaine et al. (2002) $M_{\text{BH}}-\sigma_*$ relation.

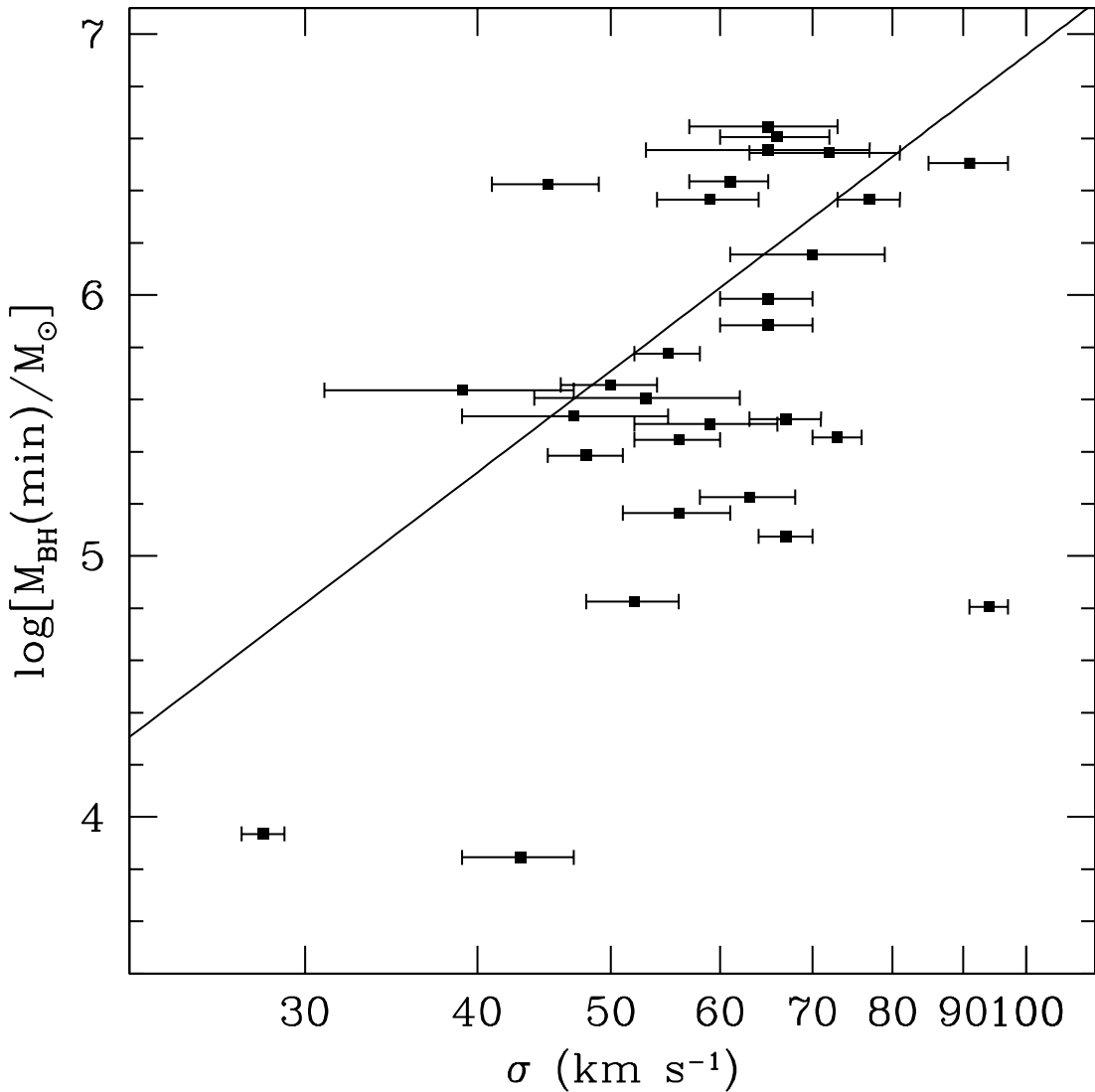


FIG. 15.— Minimum black hole mass vs. stellar velocity dispersion, assuming that the black holes are radiating at $L_{\text{bol}}/L_{\text{Edd}} < 1$, and assuming a bolometric correction of $L_{\text{bol}}/L([\text{O III}]) = 3500$. For the two galaxies lacking measurements of σ_* , the quantity $\text{FWHM}([\text{O III}])/2.35$ has been used in place of the stellar velocity dispersion. The solid line is the $M_{\text{BH}} - \sigma_*$ relation from Tremaine et al. (2002).

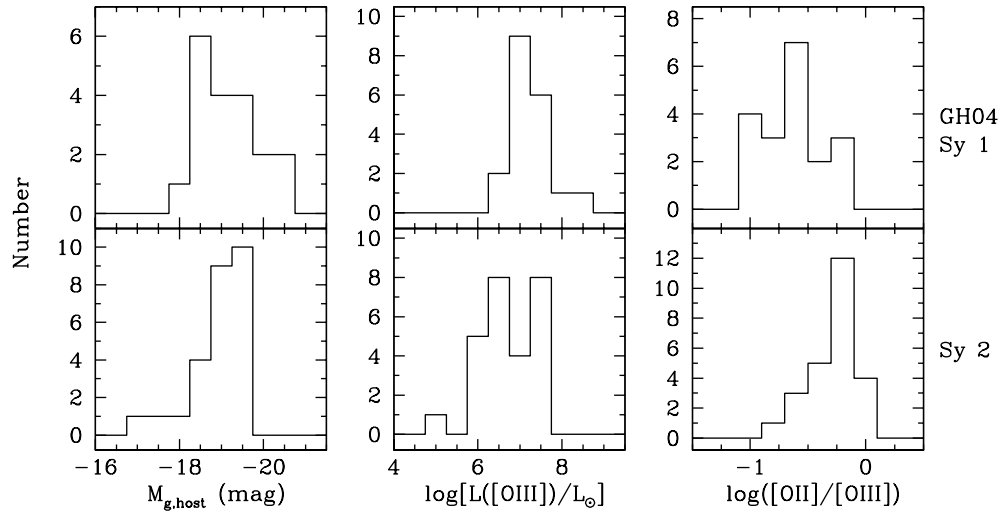


FIG. 16.— Histograms of host galaxy absolute magnitude M_g , [O III] luminosity, and $\log([\text{O II}] \lambda 3727 / [\text{O III}] \lambda 5007)$ for the Greene & Ho (2004) Seyfert 1 sample (upper panels) and the Seyfert 2 sample described in this paper (lower panels).